Universität Karlsruhe (TH)
Institut für Baustatik

A piezoelectric 3D-beam finite element formulation accounting for geometrical and material nonlinearities

A. Butz, S. Klinkel, W. Wagner

Mitteilung 4(2007)

Universität Karlsruhe (TH)
Institut für Baustatik

A piezoelectric 3D-beam finite element formulation accounting for geometrical and material nonlinearities

A. Butz, S. Klinkel, W. Wagner

Mitteilung 4(2007)

Prof. Dr.–Ing. W. Wagner
Institut für Baustatik
Universität Karlsruhe
Postfach 6980
76128 Karlsruhe

Telefon: (0721) 608–2280
Telefax: (0721) 608–6015
E–mail: bs@.uni-karlsruhe.de
Internet: http://www.bs.uni-karlsruhe.de

A piezoelectric 3D-beam finite element formulation accounting for geometrical and material nonlinearities

A. Butz[1], S. Klinkel[2] and W. Wagner[2]

[1]Fraunhofer Institut für Werkstoffmechanik IWM, Woehlerstr. 11, 79108 Freiburg, Germany

[2]Institut für Baustatik, Universität Karlsruhe (TH), Kaiserstr. 12, 76131 Karlsruhe, Germany

Abstract

The paper is concerned with a 3D piezoelectric beam formulation and its finite element implementation. The developed model considers geometrically and materially nonlinear effects. An eccentric beam formulation is derived based on the Timoshenko kinematic assumptions. These are extended by additional warping functions of the cross section, which follow from torsionally and piezoelectrically induced shear deformations. The formulation incorporates large displacements and finite rotations and allows the investigation of stability problems. The finite element model has two nodes with nine mechanical and five electrical degrees of freedom. It provides an accurate approximation of the electric potential which is assumed to be quadratic through the cross section. The mechanical degrees of freedom are displacements, rotations and scaling factors for the warping functions. The latter are computed in a preprocess solving a 2D in-plane equilibrium condition with the finite element method. The gained warping patterns are considered within the integration through the cross section of the beam formulation. With respect to material nonlinearities, which arise in ferroelectric materials, the Preisach model is embedded in the formulation. Its application to piezoelectric materials leads to a phenomenological model for ferroelectric hysteresis effects. Some examples demonstrate the capability of the proposed model.

Contents

1 INTRODUCTION **3**

2 GOVERNING EQUATIONS FOR PIEZOELECTRICITY **5**

3 FERROELECTRIC HYSTERESIS PHENOMENA USING THE PREISACH MODEL **6**

3.1 General description of the Preisach Model 6

3.2 Specification of the Preisach model to account for ferroelectric material behavior 7

4 BASIC ASSUMPTIONS FOR THE PIEZOELECTRIC BEAM FORMULATION **8**

4.1 Condensation of the constitutive equations 8

4.2 Kinematic description of the beam 9

4.3 Evaluation of the warping functions 11

4.4 Electric field quantities 13

5 VARIATIONAL FORMULATION **13**

5.1 Internal virtual work 14

5.2 External virtual work 15

5.3 Linearization of the virtual work expressions 16

6 FINITE ELEMENT APPROXIMATION **18**

7 NUMERICAL EXAMPLES **21**

7.1 Ferroelectric Hysteresis 22

7.2 Shear actuator 24

7.3 Torsional actuator 26

7.4 Piezoelectric switch 28

7.5 Helical spring 30

8 CONCLUSIONS **34**

A Material data **35**

A.1 Example 7.1 35

A.2 Example 7.2 and 7.3 35

A.3 Example 7.4 35

A.4 Example 7.5 35

1 INTRODUCTION

Piezoelectric devices are found in a wide range of applications for sensing and actuation in the field of smart materials and structures, see e.g. [50, 54]. A lot of these devices have the shape of beam structures, e.g. the shear actuator in [4] or the acceleration sensor in [15]. These systems are capable to measure forces in the range of millinewton up to kilonewton and displacements are detected with an accuracy in the range of micrometers, see [57]. Due to the high accuracy the present work is motivated by the need to analyze the stress and deformation state of the piezoelectric beam structure as precisely as possible.

A well established tool to solve the electromechanical coupled boundary value problem is the finite element method. In [6] a survey of finite element formulations is given for piezoelectric solid, shell and beam structures. The beam models are restricted to some basic assumptions regarding the dimensional formulation, geometrical nonlinearities, material nonlinearities and the description of cross section deformations.

Most piezoelectric beam theories are based on a two-dimensional approach, which is sufficient if simple problems like the bending actuator problem are analyzed. For layered piezoelectric devices with anisotropic material behavior a two-dimensional approach is not a satisfactory model. Here, coupling effects like bending and torsion coupling, see e.g. [28], may be obtained. This necessitates a three-dimensional formulation for piezoelectric beam structures. Another argument for three-dimensional models are actuators or sensors which operate in torsional mode, see [7]. Some modern actuators possess an initial spatial structure, for instance the helical spring actuator described in [40, 41]. However, in the literature only a few contributions concerning with three-dimensional piezoelectric beam structures are found. Jiao and Zhang [25] analyze a helical spring with a simplified analytical formulation. In [2] a reduced kinematic is suggested to investigate the bending torsion coupling in laminated piezoelectric devices. Ganapathi et al. [17] suggested a three-dimensional formulation with a warping function for torsion, which is restricted to rectangular cross sections and linear problems.

A geometrically nonlinear formulation is necessary to describe stability effects. In the work of [22, 37] the piezoelectric effect is utilized to strengthen the structure and to increase the stability load. Closed solutions are presented. In [13, 36] the significant impact of geometrically nonlinearities for 2D structures is discussed.

Material nonlinearities arise in ferroelectric ceramics. These class of materials is preferred for the industrial production of piezoelectric devices. It is characterized by significant ferroelastic and ferroelectric hysteresis effects. In recent years some thermodynamic constitutive models have been developed, see [26, 27] or [31] and the references therein. A very simple model to capture arbitrary hysteresis effects is the so-called Preisach model, introduced in [43]. The model needs only a few material parameters and was originally developed to describe effects arising in magnetization processes. In recent years the model is successfully

adopted to model ferroelectric ceramics, see e.g. [12, 23, 39, 49, 60]. Hwang et al. [23] employed the Preisach model to predict the remanent polarization and the remanent strain from an imposed electric field and a stress. They introduced a simple fully coupled one-dimensional model with uni-axial loading. In [39, 49, 60] the Preisach model is utilized to account only for the dielectric hysteresis. Here, the Preisach approach is implemented in a three-dimensional beam finite element to model the dielectric and the butterfly hysteresis.

Due to the fact that the piezoelectric devices have traditionally laminate forms, the above mentioned beam formulations include a more or less sophisticated laminate theory. A survey of different laminate theories is given in [46]. The simplest theory considers the strain which arise due to the piezoelectric effect as additional strain, no electric freedom is taken into account. Enhanced formulations include the electric potential as degree of freedom. The so-called equivalent single-layer models are based on the assumption that the whole cross-section deforms like one layer. More sophisticated models consider the kinematics and the variation of the electric potential through the thickness as piecewise continuous, see e.g. [45]. These theories are able to account for higher order effects, but they are expensive from a computational point of view.

The essential features and novel aspects of the present work are summarized as follows:

- On the basis of the Timoshenko kinematic assumptions an eccentric beam formulation for piezoelectric structures is derived. These assumptions are extended by three additional warping functions of the cross section. For the finite element approximation an element with two nodes and nine mechanical and five electric degrees of freedom per node is used. The mechanical degrees of freedom are three displacements, three rotations and three scaling factors for the warping patterns. The five electric degrees of freedom are employed for a sufficiently accurate approximation of the electric potential.

- The geometrically nonlinear theory accounts for large displacements and rotations and is able to represent rigid body motions and to analyze stability problems.

- The constitutive relation is based on a piezoelectric continuum formulation. In the frame of beam theory the stress components perpendicular to the beam axis are assumed to be zero. The corresponding material matrix is observed by a static condensation. With respect to the material nonlinearities the Preisach model is implemented. The three-dimensional uniaxial model is able to represent the ferroelectric hysteresis and the so-called butterfly loop.

- The deformations of the cross section are analyzed in a preprocess and result in warping patterns. A two-dimensional boundary value problem is solved by the finite element method. The warping functions follow from torsion and piezoelectrically induced shear deformations. An arbitrary cross section consisting out of different layers

is modeled by quadrilateral elements. The resulting warping patterns are incorporated in the beam formulation; in particular the finite element mesh is employed for the integration through the cross section. The suggested formulation may be seen as an alternative to the so-called discrete layer models.

The outline of the paper is as follows: In Section 2 the governing equations of the electromechanically coupled boundary value problem are derived. In Section 3 the Preisach model is described and adopted for the electromechanical boundary problem. Section 4 is concerned with the basic assumptions of the piezoelectric beam formulation regarding the constitutive law, the kinematic description and the distribution of the electric field through the cross section. In the next Section the variational formulation is described. In Section 6 the finite element approximation is introduced. Finally, in Section 7 some numerical examples show the capability of the presented formulation.

2 GOVERNING EQUATIONS FOR PIEZOELECTRICITY

In this section the basic equations for piezoelectricity are briefly summarized to clarify the notation. These equations are fundamental for the subsequent finite beam element formulation. The equilibrium equation and the local form of Gauss law with respect to the reference configuration $\mathcal{B}_0$ are given as

$$\operatorname{Div} \boldsymbol{P} + \boldsymbol{b} = 0 \qquad \text{in} \quad \mathcal{B}_0 \tag{1}$$

$$\operatorname{Div} \vec{\boldsymbol{D}} = 0 \qquad \text{in} \quad \mathcal{B}_0 \quad . \tag{2}$$

Here, $\boldsymbol{P}$ denotes the first Piola-Kirchhoff stress tensor and my be expressed as $\boldsymbol{P} = \boldsymbol{F}\,\boldsymbol{S}$, where $\boldsymbol{F} = \operatorname{Grad} \boldsymbol{x}$ is the deformation gradient and $\boldsymbol{S}$ is the second Piola-Kirchhoff stress tensor. The Vector $\boldsymbol{b}$ describes the mechanical body forces. $\vec{\boldsymbol{D}}$ corresponds to the dielectric displacements, free volume charges are not considered in Eq. (2). The mechanical and electrical boundary conditions read

$$\boldsymbol{S} \cdot \boldsymbol{n} - \boldsymbol{t} = 0 \qquad \text{on} \quad \partial_t \mathcal{B}_0 \tag{3}$$

$$\vec{\boldsymbol{D}} \cdot \boldsymbol{n} - \bar{\sigma} = 0 \qquad \text{on} \quad \partial_\sigma \mathcal{B}_0 \quad , \tag{4}$$

in which $\boldsymbol{t}$ is defined as the prescribed traction vector on the surface $\partial_t \mathcal{B}_0$ and the scalar value $\bar{\sigma}$ is the electric surface charge on $\partial_\sigma \mathcal{B}_0$. The outward unit normal vector on $\partial \mathcal{B}_0$ is denoted by $\boldsymbol{n}$. The geometrically nonlinear Green-Lagrangean strains $\boldsymbol{E}$ and the electric field $\vec{\boldsymbol{E}}$ are defined as

$$\boldsymbol{E} = \frac{1}{2}(\operatorname{Grad} \boldsymbol{u} + \operatorname{Grad} \boldsymbol{u}^T + \operatorname{Grad} \boldsymbol{u}^T \ \operatorname{Grad} \boldsymbol{u}) \tag{5}$$

$$\vec{\boldsymbol{E}} = -\operatorname{Grad} \phi \quad , \tag{6}$$

where $\boldsymbol{u}$ is the displacement vector and ϕ is the electric potential. In order to include nonlinear material behavior which is caused by piezoelectric domain switching effects, the irreversible or remanent polarization vector $\vec{\boldsymbol{P}}^i$ is introduced. It serves as an internal state variable. Due to the domain switching an irreversible strain $\boldsymbol{E}^i$ arises. The nonlinear constitutive equations are given as

$$\begin{aligned} \boldsymbol{S} &= \mathbb{C}(\vec{\boldsymbol{P}}^i) : (\boldsymbol{E} - \boldsymbol{E}^i) - \mathbb{e}(\vec{\boldsymbol{P}}^i) \cdot \vec{\boldsymbol{E}} \\ \vec{\boldsymbol{D}} - \vec{\boldsymbol{P}}^i &= \mathbb{e}(\vec{\boldsymbol{P}}^i)^T : (\boldsymbol{E} - \boldsymbol{E}^i) + \boldsymbol{\epsilon}(\vec{\boldsymbol{P}}^i) \cdot \vec{\boldsymbol{E}} \quad . \end{aligned} \tag{7}$$

Here, $\mathbb{C}$, $\mathbb{e}$ and $\boldsymbol{\epsilon}$ are the elasticity tensor, the piezoelectric tensor and the permittivity tensor as functions of the internal state variable. In this work only ferroelectric hysteresis phenomena are considered. In this case the remanent polarization depends only on the electric field $\vec{\boldsymbol{P}}^i = \vec{\boldsymbol{P}}^i(\vec{\boldsymbol{E}})$. This relation will be discussed in detail within the Preisach model in the next section.

3 FERROELECTRIC HYSTERESIS PHENOMENA USING THE PREISACH MODEL

The Preisach model [43] was introduced in 1935 to describe hysteresis effects in magnetic materials. The Russian mathematician Krasnoselski [29] separated the Preisach model from its physical meaning. It is a general and fundamental mathematical formulation, which is able to describe a wide range of different hysteresis phenomena. The most important nonlinear material parameter of this model is the so-called Preisach function. Several identification procedures for its determination are proposed in the literature, see e.g. [14, 24, 33]. An implementation of the Preisach model in the subsequent finite element formulation is derived. First, a brief description of the basic idea of the Preisach model is presented, for detailed information see Mayergoyz [33]. In a second step the application to ferroelectric hysteresis effects is described.

3.1 General description of the Preisach Model

The basic idea of the Preisach model states, that a complex hysteresis can be composed by the superposition of an infinite number of simple elementary hysteresis operators or hysterons $\gamma_{\alpha\beta}$. Each operator corresponds to a simple rectangular loop of an input-output diagram as depicted in Fig. 1. The output value $\gamma_{\alpha\beta}(u)$ of one single hysteron is $+1$ or -1. For a monotone increasing of the input value $u(t)$, the output value follows the path $ABCDE$. Vice versa, in the case of a monotone decreasing value $u(t)$, $\gamma_{\alpha,\beta}(u)$ follows the path $EDFBA$. The parameters α and β describe to up- and down-switching values that cause a change of $\gamma_{\alpha\beta}(u)$ from -1 or $+1$ and $+1$ or -1, respectively. Each hysteron has specific values for

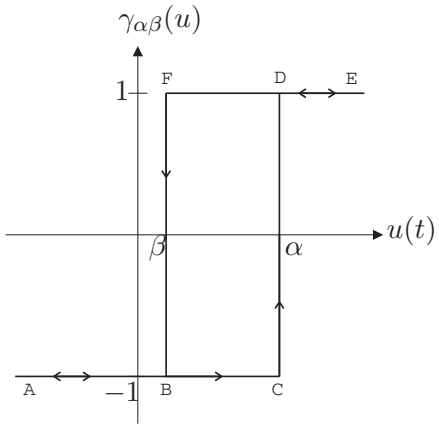

Figure 1: Input-Output diagram of a single hysteron.

α and β. Thereby, α and β can be positive or negative with the constraint $\alpha \geq \beta$. The global output value is obtained by the superposition of all output values with the following integration

$$f(t) = \iint\limits_{\alpha \geq \beta} \mu(\alpha, \beta)\, \gamma_{\alpha\beta}(u(t))\ \mathrm{d}\,\alpha\ \mathrm{d}\,\beta \quad . \tag{8}$$

The expression $\mu(\alpha, \beta)$ is called the Preisach function and can be treated as a weighting function for each hysteron. On this note, the condition

$$\iint\limits_{\alpha \geq \beta} \mu(\alpha, \beta)\ \mathrm{d}\,\alpha\ \mathrm{d}\,\beta = 1 \tag{9}$$

must be fulfilled. Further, the normalization of the input value leads to the following definition of the Preisach function

$$\mu(\alpha, \beta) = \begin{cases} \mu(\alpha, \beta) & \text{; if} \quad -1 \leq \alpha \leq 1 \quad \text{and} \quad -1 \leq \beta \leq \alpha \\ 0 & \text{; otherwise .} \end{cases} \tag{10}$$

3.2 Specification of the Preisach model to account for ferroelectric material behavior

For the application of the Preisach model to beam formulations the following assumptions are made:

- The irreversible polarization $\vec{\boldsymbol{P}}^i$ is determined by the Preisach model. The orientation of the irreversible polarization is arbitrary but fixed and corresponds to the direction of the external electric field. Thus, this model is restricted to 180 degree domain switching effect.

- Only the components of the irreversible beam strains are considered, which appear in the beam formulation.
- Ferroelastic hysteresis phenomena are not taken into account in this work.

The global output function $f(t)$ of the Preisach model corresponds to the relative, irreversible polarization $\vec{P}^{i,rel}$ which is defined in $-1 \leq \vec{P}^{i,rel} \leq 1$. It describes the fraction of the piezoelectric material that exhibits a macroscopic polarization. The algebraic sign defines the direction of the irreversible polarization. The value of the resulting irreversible polarization $\vec{P}^{i}$ is given by the equation

$$\vec{\boldsymbol{P}}^{\,i} = \vec{P}^{sat}\, \vec{P}^{i,rel} \boldsymbol{e}^{P} \tag{11}$$

with the saturation polarization $\vec{P}^{sat}$ and the prescribed direction of the irreversible polarization defined by the unit vector $\boldsymbol{e}^{P}$. Since the domain switching effects can be treated as a volume conserving process [23], the irreversible strains $\boldsymbol{E}^{i}$ are determined as proposed by Kamlah [26] and McMeeking & Landis [34]

$$\boldsymbol{E}^{i} = \frac{3}{2}\, E^{sat}\, \frac{\|\vec{\boldsymbol{P}}^{\,i}\|}{\vec{P}^{sat}} \left(\boldsymbol{e}^{P} \otimes \boldsymbol{e}^{P} - \frac{1}{3}\, \boldsymbol{I}\right) \quad . \tag{12}$$

The irreversible beam strains consider the components $\boldsymbol{E}^{i}_{b} = [E^{i}_{11}, 2\, E^{i}_{12}, 2\, E^{i}_{13}]$ and follow from Eq. (12) as

$$\boldsymbol{E}^{i}_{b} = E^{sat}\, \vec{P}^{i,rel} \begin{bmatrix} \frac{3}{2}\, e^{P}_{1}\, e^{P}_{1} - \frac{1}{2} \\ 3\, e^{P}_{1}\, e^{P}_{2} \\ 3\, e^{P}_{1}\, e^{P}_{3} \end{bmatrix} \tag{13}$$

Due to the poling process, the piezoelectric material has orthotropic properties. Thus, the matrices $\tilde{\mathbb{C}}$, $\tilde{\mathfrak{e}}$ and $\tilde{\boldsymbol{\epsilon}}$ must be transformed in direction of the vector $\boldsymbol{e}^{P}$. This transformation can be performed by standard operations and will not be discussed in this paper.

4 BASIC ASSUMPTIONS FOR THE PIEZOELECTRIC BEAM FORMULATION

4.1 Condensation of the constitutive equations

The special stress assumption in beam theory ($\boldsymbol{S}_{k} = [S_{22}, S_{33}, S_{23}]^{T} = 0$) requires a modification of the three-dimensional constitutive equations given in Eq. (7). Introducing the stress vector $\boldsymbol{S}_{b} = [S_{11}, S_{12}, S_{13}]^{T}$ and the corresponding strain vectors $\boldsymbol{E}_{b} = [E_{11}, 2\, E_{12}, 2\, E_{13}]^{T}$ and $\boldsymbol{E}_{k} = [E_{22}, E_{33}, 2\, E_{23}]^{T}$, the constitutive equation is rewritten as

$$\begin{bmatrix} \boldsymbol{S}_{b} \\ \boldsymbol{S}_{k} \\ \vec{\boldsymbol{D}} - \vec{\boldsymbol{P}}^{\,i} \end{bmatrix} = \begin{bmatrix} \mathbb{C}_{b} & \mathbb{C}_{bk} & -\mathfrak{e}_{b} \\ \mathbb{C}^{T}_{bk} & \mathbb{C}_{k} & -\mathfrak{e}_{k} \\ \mathfrak{e}^{T}_{b} & \mathfrak{e}^{T}_{k} & \boldsymbol{\epsilon} \end{bmatrix} \begin{bmatrix} \boldsymbol{E}_{b} - \boldsymbol{E}^{i}_{b} \\ \boldsymbol{E}_{k} - \boldsymbol{E}^{i}_{k} \\ \vec{\boldsymbol{E}} \end{bmatrix} \quad . \tag{14}$$

Considering the assumption $\boldsymbol{S}_k = \boldsymbol{0}$, the strains $\boldsymbol{E}_k$ can be eliminated from the constitutive equations by static condensation which leads to

$$\begin{aligned} \boldsymbol{S}_b &= \tilde{\mathbb{C}}(\vec{\boldsymbol{P}}^i)\,(\boldsymbol{E}_b - \boldsymbol{E}_b^i) - \tilde{\mathfrak{e}}(\vec{\boldsymbol{P}}^i)\,\vec{\boldsymbol{E}} \\ \vec{\boldsymbol{D}} - \vec{\boldsymbol{P}}^i &= \tilde{\mathfrak{e}}(\vec{\boldsymbol{P}}^i)^T\,(\boldsymbol{E}_b - \boldsymbol{E}_b^i) + \tilde{\boldsymbol{\epsilon}}(\vec{\boldsymbol{P}}^i)\,\vec{\boldsymbol{E}} \quad , \end{aligned} \tag{15}$$

with

$$\tilde{\mathbb{C}} := \mathbb{C}_b - \mathbb{C}_{bk}\,\mathbb{C}_k^{-1}\,\mathbb{C}_{bk}^T \qquad \tilde{\mathfrak{e}} := \mathfrak{e}_b - \mathbb{C}_{bk}\,\mathbb{C}_k^{-1}\,\mathfrak{e}_k \qquad \tilde{\boldsymbol{\epsilon}} := \boldsymbol{\epsilon} + \mathfrak{e}_k^T\,\mathbb{C}_k^{-1}\,\mathfrak{e}_k \quad . \tag{16}$$

The condensation of the three-dimensional constitutive law is a standard procedure, see e.g. Benjeddou et al. [8], who assumed a special poling direction of the piezoelectric material. In this work, an arbitrary poling direction of the piezoelectric material is taken into account. This is especially advantageous for three-dimensional structures, see also Section 7.

4.2 Kinematic description of the beam

The kinematic description is based on the work by Gruttmann et al. [19, 21] which is adjusted to the special requirements of the presented piezoelectric beam formulation. Therefore, we make the following assumptions:

- For the kinematic description the Timoshenko beam theory is employed and enhanced by three additional warping functions.
- The shape of the cross section remains unchanged during the deformation of the beam.
- The cross sections are thick-walled.
- The mechanical loads are assumed to be conservative. The electric loading described in Section 4.4 is defined with respect to the local beam axis of the undeformed configuration.
- The kinematic description considers large deformations but small strains.

A beam in the reference configuration $\mathcal{B}_0$ and in the current configuration $\mathcal{B}_t$ is shown in Fig. 2. To describe an arbitrary point of the beam in $\mathcal{B}_0$, an orthogonal coordinate system $\boldsymbol{A}_i$ is introduced. In the reference configuration the basis vector $\boldsymbol{A}_1$ corresponds to the coordinate $S = \xi_1 \in [0, L]$. The cross section is in plane and described by the vectors $\boldsymbol{A}_2$ and $\boldsymbol{A}_3$. The coordinate system $\boldsymbol{a}_i$ in the current configuration $\mathcal{B}_t$ has also orthogonal base vectors. Due to the beam kinematics the vector $\boldsymbol{a}_1$ is not necessarily the tangent vector of the deformed reference curve. The vectors $\boldsymbol{X}_0$ and $\boldsymbol{x}_0$ define an arbitrary point on the reference

line. Its displacement $\boldsymbol{u}$ is given by $\boldsymbol{u} = \boldsymbol{x}_0 - \boldsymbol{X}_0$. By introducing the global cartesian coordinate system $\boldsymbol{e}_i$ the base vectors $\boldsymbol{A}_i$ and $\boldsymbol{a}_i$ follow from the orthogonal transformation

$$\boldsymbol{A}_i(S) = \boldsymbol{R}_0(S)\, \boldsymbol{e}_i \qquad \boldsymbol{a}_i(S,t) = \boldsymbol{R}(S,t)\, \boldsymbol{e}_i \quad \text{with} \quad \boldsymbol{R},\, \boldsymbol{R}_0 \in SO(3) \quad . \tag{17}$$

The rotation tensors $\boldsymbol{R}_0$ and $\boldsymbol{R}$ are described by an axial vector with three parameters, see also e.g. [52].

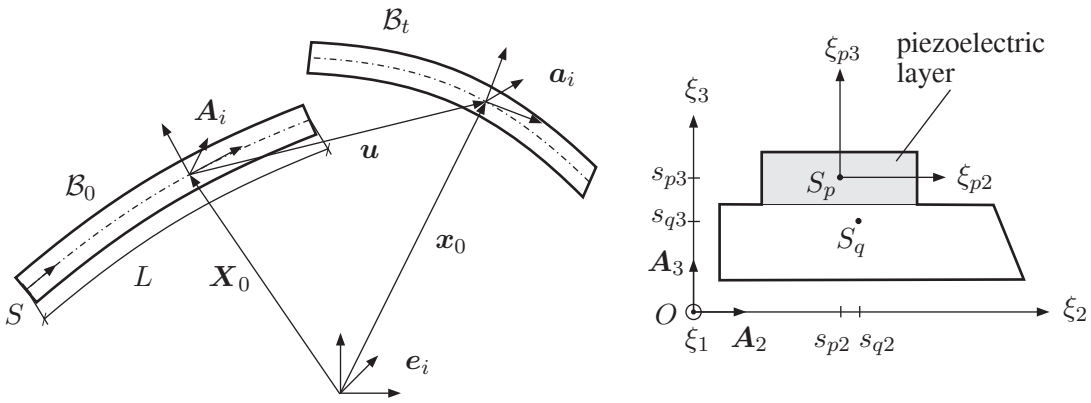

Figure 2: Beam configuration and definition of the cross section.

An arbitrary point of the beam is defined by the position vectors $\boldsymbol{X}$ and $\boldsymbol{x}$ in the reference and the current configuration respectively

$$\boldsymbol{X}(\xi_2,\xi_3,S) = \boldsymbol{X}_0(S) + \xi_2\, \boldsymbol{A}_2(S) + \xi_3\, \boldsymbol{A}_3(S)$$

$$\boldsymbol{x}(\xi_2,\xi_3,S,t) = \boldsymbol{x}_0(S,t) + \xi_2\, \boldsymbol{a}_2(S,t) + \xi_3\, \boldsymbol{a}_3(S,t) + [\bar{\bar{\boldsymbol{\omega}}}(\xi_2,\xi_3)\cdot\boldsymbol{\alpha}(S,t)]\, \boldsymbol{a}_1(S,t) \quad . \tag{18}$$

The vector $\bar{\bar{\boldsymbol{\omega}}}$ contains the values of the three warping functions at the cross section coordinates (ξ_2,ξ_3). Each warping function is multiplied with a separate scaling factor $\alpha_i,\ i = 1...3$. They are arranged in the vector $\boldsymbol{\alpha} = [\alpha_1,\alpha_2,\alpha_3]^T$. Here the base vector $\boldsymbol{a}_1$ is assumed to be piecewise constant, see [20]. The evaluation of the warping functions is discussed in Section 4.3 in detail.

Based on the kinematic assumptions (18), the tangent vectors $\boldsymbol{G}_i = \boldsymbol{X}_{,i}$ and $\boldsymbol{g}_i = \boldsymbol{x}_{,i}$ are given as

$$\begin{aligned} \boldsymbol{G}_1 &= \boldsymbol{X}_0' + \xi_2\, \boldsymbol{A}_2' + \xi_3\, \boldsymbol{A}_3' & \boldsymbol{g}_1 &= \boldsymbol{x}_0' + \xi_2\, \boldsymbol{a}_2' + \xi_3\, \boldsymbol{a}_3' + \bar{\bar{\boldsymbol{\omega}}}\cdot\boldsymbol{\alpha}'\, \boldsymbol{a}_1 \\ \boldsymbol{G}_2 &= \boldsymbol{A}_2 & \boldsymbol{g}_2 &= \boldsymbol{a}_2 + (\bar{\bar{\boldsymbol{\omega}}}_{,2}\cdot\boldsymbol{\alpha})\, \boldsymbol{a}_1 \\ \boldsymbol{G}_3 &= \boldsymbol{A}_3 & \boldsymbol{g}_3 &= \boldsymbol{a}_3 + (\bar{\bar{\boldsymbol{\omega}}}_{,3}\cdot\boldsymbol{\alpha})\, \boldsymbol{a}_1 \quad . \end{aligned} \tag{19}$$

The expression $(\cdot)'$ denotes the differentiation with respect to the beam coordinate S. The derivatives of the base vectors are determined as

$$\boldsymbol{A}_i' = \boldsymbol{R}_0'\, \boldsymbol{R}_0^T\, \boldsymbol{A}_i \qquad \boldsymbol{a}_i' = \boldsymbol{R}'\, \boldsymbol{R}^T\, \boldsymbol{a}_i \quad . \tag{20}$$

The tensor products $\boldsymbol{R}_0' \ \boldsymbol{R}_0^T$ and $\boldsymbol{R}' \ \boldsymbol{R}^T$ yield a skew symmetric tensor. Accordingly, Eqs. (20) can be written alternatively as

$$\boldsymbol{A}_i' = \boldsymbol{\theta}_0 \times \boldsymbol{A}_i \qquad\qquad \boldsymbol{a}_i' = \boldsymbol{\theta} \times \boldsymbol{a}_i \quad , \tag{21}$$

with the axial vectors $\boldsymbol{\theta}_0$ and $\boldsymbol{\theta}$ respectively. With respect to small strains, the Green-Lagrangean strains are taken into account and are derived using the tangent vectors given in Eq. (19), see also [19],

$$E_{ij} = \frac{1}{2}\left(\boldsymbol{x}_{,i} \cdot \boldsymbol{x}_{,j} - \boldsymbol{X}_{,i} \cdot \boldsymbol{X}_{,j}\right) = \frac{1}{2}\left(\boldsymbol{g}_i \cdot \boldsymbol{g}_j - \boldsymbol{G}_i \cdot \boldsymbol{G}_j\right) \quad . \tag{22}$$

Within the framework of the beam formulation, the resulting strain tensor is reduced to the vector $\boldsymbol{E}_b = [E_{11}, 2\,E_{12}, 2\,E_{13}]^T$ and decomposed as follows

$$\boldsymbol{E}_b = \widehat{\boldsymbol{A}}(\xi_2, \xi_3)\, \widehat{\boldsymbol{E}}(S) \quad . \tag{23}$$

The mechanical transformation matrix $\widehat{\boldsymbol{A}}(\xi_2, \xi_3)$ contains the quantities that depend on the cross section coordinates ξ_2 and ξ_3

$$\widehat{\boldsymbol{A}}(\xi_2, \xi_3) = \begin{bmatrix} 1 & 0 & 0 & 0 & \xi_3 & -\xi_2 & 0 & 0 & 0 & \bar{\omega}_1 & \bar{\omega}_2 & \bar{\omega}_3 \\ 0 & 1 & 0 & -\xi_3 & 0 & 0 & \bar{\omega}_{1,2} & \bar{\omega}_{2,2} & \bar{\omega}_{3,2} & 0 & 0 & 0 \\ 0 & 0 & 1 & \xi_2 & 0 & 0 & \bar{\omega}_{1,3} & \bar{\omega}_{2,3} & \bar{\omega}_{3,3} & 0 & 0 & 0 \end{bmatrix} \quad , \tag{24}$$

whereas the beam strains are arranged in the vector $\widehat{\boldsymbol{E}}(S)$

$$\widehat{\boldsymbol{E}}(S) = \begin{bmatrix} \boldsymbol{\varepsilon} - \boldsymbol{\varepsilon}_0 \\ \boldsymbol{\kappa} - \boldsymbol{\kappa}_0 \\ \boldsymbol{\alpha} \\ \boldsymbol{\alpha}' \end{bmatrix} \quad . \tag{25}$$

Using the small strain assumption, higher order products of ξ_2, ξ_3, $\bar{\omega}_i$, α_i and α_i' can be neglected. This leads to the following strain measures

$$\boldsymbol{\varepsilon} = \begin{bmatrix} \frac{1}{2}\,\boldsymbol{x}_0' \cdot \boldsymbol{x}_0' \\ \boldsymbol{x}_0' \cdot \boldsymbol{a}_2 \\ \boldsymbol{x}_0' \cdot \boldsymbol{a}_3 \end{bmatrix} \qquad\qquad \boldsymbol{\kappa} = \begin{bmatrix} \boldsymbol{\theta} \cdot \boldsymbol{a}_1 \\ \boldsymbol{x}_0' \cdot \boldsymbol{a}_3' \\ \boldsymbol{x}_0' \cdot \boldsymbol{a}_2' \end{bmatrix} \quad . \tag{26}$$

The strain measure $\boldsymbol{\varepsilon}_0$ and $\boldsymbol{\kappa}_0$ result from Eq. (26) if the base vectors of the current configuration are replaced by the base vectors of the reference configuration.

4.3 Evaluation of the warping functions

The evaluation of cross-section warping for torsional problems is a classical problem in mechanics, see [56]. For electromechanical problems the situation is more complex due to

the fact that warping induced by electrical loading occur. To the knowledge of the authors this problem is not discussed in the literature up to now. However, here cross-section warping due to piezoelectric shear actuation is analyzed. The warping patterns are determined by the Neumann problem

$$\begin{aligned} S_{12,2} + S_{13,3} &= 0 \qquad \text{in} \quad \Omega \\ S_{12}\, n_2 + S_{13}\, n_3 &= 0 \qquad \text{on} \quad \partial\Omega \quad . \end{aligned} \tag{27}$$

For the torsional problem, we prescribe an unit torque of the beam axis. Under consideration of a geometrically linear kinematic, the resulting shear stresses are given as

$$\begin{bmatrix} S_{12} \\ S_{13} \end{bmatrix} = \begin{bmatrix} \tilde{\mathbb{C}}_{22} & \tilde{\mathbb{C}}_{23} \\ \tilde{\mathbb{C}}_{32} & \tilde{\mathbb{C}}_{33} \end{bmatrix} \begin{bmatrix} \omega_{1,2} - \xi_3 \\ \omega_{1,3} + \xi_2 \end{bmatrix} \quad , \tag{28}$$

where ω_1 denotes the warping due to torsion. The piezoelectrically induced shear deformation leads to constant shear strains $2E_{12}$, $2E_{13}$ in the piezoelectric layer. These are prescribed as unit shear strains to the piezoelectric cross section. The resulting shear stresses read

$$\begin{bmatrix} S_{12} \\ S_{13} \end{bmatrix} = \begin{bmatrix} \tilde{\mathbb{C}}_{22} & \tilde{\mathbb{C}}_{23} \\ \tilde{\mathbb{C}}_{32} & \tilde{\mathbb{C}}_{33} \end{bmatrix} \begin{bmatrix} \omega_{2,2} + 1 \\ \omega_{2,3} \end{bmatrix} \quad , \quad \begin{bmatrix} S_{12} \\ S_{13} \end{bmatrix} = \begin{bmatrix} \tilde{\mathbb{C}}_{22} & \tilde{\mathbb{C}}_{23} \\ \tilde{\mathbb{C}}_{32} & \tilde{\mathbb{C}}_{33} \end{bmatrix} \begin{bmatrix} \omega_{3,2} \\ \omega_{3,3} + 1 \end{bmatrix} \quad . \tag{29}$$

The ω_i with i denote the three cases which describe the warping due to torsion and piezoelectrically shear actuation in ξ_2- and ξ_3-direction, respectively. The weak formulation of Eq. (27), with respect to the three loads cases reads

$$\int_\Omega \begin{bmatrix} \delta\omega_{i,2} \\ \delta\omega_{i,3} \end{bmatrix}^T \left(\begin{bmatrix} \tilde{\mathbb{C}}_{22} & \tilde{\mathbb{C}}_{23} \\ \tilde{\mathbb{C}}_{32} & \tilde{\mathbb{C}}_{33} \end{bmatrix} \begin{bmatrix} \omega_{i,2} \\ \omega_{i,3} \end{bmatrix} + \begin{bmatrix} \tilde{\mathbb{C}}_{22} & \tilde{\mathbb{C}}_{23} \\ \tilde{\mathbb{C}}_{32} & \tilde{\mathbb{C}}_{33} \end{bmatrix} \boldsymbol{f}_i \right) \mathrm{d}\, A = 0 \tag{30}$$

with

$$\boldsymbol{f}_1 = \begin{bmatrix} -\xi_3 \\ \xi_2 \end{bmatrix}, \quad \boldsymbol{f}_2 = \begin{bmatrix} 1 \\ 0 \end{bmatrix}, \quad \boldsymbol{f}_3 = \begin{bmatrix} 0 \\ 1 \end{bmatrix} \quad . \tag{31}$$

Here, Ω is the cross-section area and $\delta\omega_i$ denotes an admissible test function. The problem is solved approximately by the finite element method. The resulting warping patterns ω_i are scaled by

$$\bar{\omega}_i = \omega_i - \frac{1}{A} \int_\Omega \omega_i \, \mathrm{d}\, A \qquad \text{with} \qquad \int_\Omega \bar{\omega}_i \, \mathrm{d}\, A = 0 \quad . \tag{32}$$

These functions are decomposed in a rigid body rotation and a part $\bar{\bar{\omega}}_i$ describing the pure warping deformation. Since the rotation is already considered in the beam kinematics, this part is eliminated by solving the minimization problem

$$\Pi = \int_\Omega \frac{1}{2} (\bar{\omega}_i(\xi_2, \xi_3) - a\, \xi_2 + b\, \xi_3)^2 \, \mathrm{d}\, A \Rightarrow \min \quad . \tag{33}$$

where a and b are parameters describing a plane. The warping function $\bar{\bar{\omega}}_i(\bar{\xi}_2, \bar{\xi}_3) = \bar{\omega}_i(\bar{\xi}_2, \bar{\xi}_3) - (a\, \bar{\xi}_2 + b\, \bar{\xi}_3)$ is incorporated in the underlying beam formulation. For a detailed description we refer to [11], [20].

4.4 Electric field quantities

Along with the kinematics of the beam formulation, an appropriate description of the electric field quantities is necessary. The choice of the approximation space for the electric potential perpendicular to the beam axis is discussed in literature in several works, see eg. Altay & Dökmeci [3], Krommer & Irschik [30] or Wang & Quek [58, 59]. Here, we use a quadratic function for the approximation of the electric potential in ξ_2- and ξ_3-direction, which reads

$$\phi(\xi_2, \xi_3, S) = c_1(S) + c_2(S)\,\xi_{p2} + c_3(S)\,\xi_{p3} + c_4(S)\left(\frac{b_p^2}{4} - \xi_{p2}^2\right) + c_5(S)\left(\frac{h_p^2}{4} - \xi_{p3}^2\right) \quad . \tag{34}$$

The quadratic terms in (34) are included for an adequate description of the electric potential in the case of bending deformations. With the proposed approximation of the electric field, the piezoelectric layer is restricted to a rectangular shape. The quantities b_p and h_p define the width and height of the piezoelectric layer, the coordinates ξ_{p2} and ξ_{p3} refer to its centroid S_p as depicted in Fig. 2. The parameters c_1 - c_5 are unknown and comply with the electrical degrees of freedom of the piezoelectric beam formulation. With respect to Eq. (34) the electric field $\vec{\boldsymbol{E}}$ Eq. (6) is determined by

$$\vec{\boldsymbol{E}} = \bar{\boldsymbol{A}}(\xi_2, \xi_3)\,\bar{\vec{\boldsymbol{E}}}(S) \quad . \tag{35}$$

The electrical transformation matrix $\bar{\boldsymbol{A}}$ is given as

$$\bar{\boldsymbol{A}}(\xi_2, \xi_3) = -\begin{bmatrix} 0 & 0 & 0 & 0 & 0 & 1 & \xi_{p2} & \xi_{p3} & \left(\frac{b_p^2}{4} - \xi_{p2}^2\right) & \left(\frac{h_p^2}{4} - \xi_{p3}^2\right) \\ 0 & 1 & 0 & -2\,\xi_{p2} & 0 & 0 & 0 & 0 & 0 & 0 \\ 0 & 0 & 1 & 0 & -2\,\xi_{p3} & 0 & 0 & 0 & 0 & 0 \end{bmatrix}, \tag{36}$$

the vector $\bar{\vec{\boldsymbol{E}}}$ contains the electric field quantities that depend on the beam coordinate S

$$\bar{\vec{\boldsymbol{E}}}(S) = \begin{bmatrix} \boldsymbol{\Phi} \\ \boldsymbol{\Phi}' \end{bmatrix} \qquad \text{with} \qquad \begin{aligned} \boldsymbol{\Phi}\,(S) &= [c_1, c_2, c_3, c_4, c_5]^T \\ \boldsymbol{\Phi}'(S) &= [c_1', c_2', c_3', c_4', c_5']^T \end{aligned} \quad . \tag{37}$$

5 VARIATIONAL FORMULATION

The weak formulation of Eqs. (1), (2) are observed integration by parts and the divergence theorem as

$$G = \int_{\mathcal{B}_0} \delta \boldsymbol{E}_b^T\, \boldsymbol{S}_b \,\mathrm{d}\,V - \int_{\mathcal{B}_0} \delta \vec{\boldsymbol{E}}^T\, \vec{\boldsymbol{D}} \,\mathrm{d}\,V - \int_{\mathcal{B}_0} \delta \boldsymbol{u}^T \boldsymbol{b} \,\mathrm{d}\,V - \int_{\partial_t \mathcal{B}_0} \delta \boldsymbol{u}^T \boldsymbol{t} \,\mathrm{d}\,A - \int_{\partial_{\bar{\sigma}} \mathcal{B}_0} \delta\phi\,\bar{\sigma} \,\mathrm{d}\,A = 0 \quad . \tag{38}$$

According to beam theory only the stresses $\boldsymbol{S}_b$ and the strains $\boldsymbol{E}_b$ are included in the virtual work expression. In the next two subsections the internal and external virtual work expressions are discussed with respect to the beam formulation, where the volume integral is split in an integral through the cross-section Ω and an integral through the beam coordinate S.

5.1 Internal virtual work

The independent kinematic quantities of the beam formulation are $\boldsymbol{v} = [\boldsymbol{u}, \boldsymbol{R}, \boldsymbol{\alpha}]^T$ with the displacements $\boldsymbol{u}$, the rotation tensor $\boldsymbol{R}$ and the scaling factors $\boldsymbol{\alpha}$ of the warping functions. The independent electric quantities are five parameters, which are summarized in the vector $\boldsymbol{\Phi} = [c_1, c_2, c_3, c_4, c_5]^T$.

Let $\mathcal{V}_v = \{\delta\boldsymbol{v} = [\delta\boldsymbol{u}, \delta\boldsymbol{w}, \delta\boldsymbol{\alpha}]^T : [0, L] \rightarrow R^3 \mid \delta\boldsymbol{v} = \boldsymbol{0} \text{ on } \partial_u\mathcal{B}\}$ be the space for admissible kinematic variation. Here, $\partial_u\mathcal{B}$ corresponds to the boundaries with prescribed displacements and rotations. The axial vector $\delta\boldsymbol{w}$ follows from $\delta\boldsymbol{a}_i = \delta\boldsymbol{R}\boldsymbol{R}^T\boldsymbol{a}_i = \delta\boldsymbol{w} \times \boldsymbol{a}_i$, see Gruttmann et al. [21]. Let $\mathcal{V}_\phi = \{\delta\boldsymbol{\Phi} : [0, L] \rightarrow R^3 \mid \delta\boldsymbol{\Phi} = \boldsymbol{0} \text{ on } \partial_\phi\mathcal{B}\}$ be the space for admissible electric potential variations. On the boundary $\partial_\phi\mathcal{B}$ the electric potential ϕ is prescribed. The virtual Green-Lagrangean strains are given as

$$\delta\boldsymbol{E} = \widehat{\boldsymbol{A}}\,\delta\widehat{\boldsymbol{E}} \qquad \text{with} \quad \delta\widehat{\boldsymbol{E}} = \begin{bmatrix}\delta\boldsymbol{\varepsilon} & \delta\boldsymbol{\kappa} & \delta\boldsymbol{\alpha} & \delta\boldsymbol{\alpha}'\end{bmatrix}^T \tag{39}$$

with the following strain components

$$\begin{aligned}
\delta\boldsymbol{\varepsilon} &= \begin{bmatrix} \boldsymbol{x}_0' \cdot \delta\boldsymbol{u}' \\ \boldsymbol{a}_2 \cdot \delta\boldsymbol{u}' + \boldsymbol{x}_0' \cdot \delta\boldsymbol{a}_2 \\ \boldsymbol{a}_3 \cdot \delta\boldsymbol{u}' + \boldsymbol{x}_0' \cdot \delta\boldsymbol{a}_3 \end{bmatrix} & \qquad \delta\boldsymbol{\alpha} &= \begin{bmatrix} \delta\alpha_1 \\ \delta\alpha_2 \\ \delta\alpha_3 \end{bmatrix} \\
\delta\boldsymbol{\kappa} &= \begin{bmatrix} \boldsymbol{a}_1 \cdot \delta\boldsymbol{\theta} \; + \boldsymbol{\theta} \cdot \delta\boldsymbol{a}_1 \\ \boldsymbol{a}_3' \cdot \delta\boldsymbol{u}' + \boldsymbol{x}_0' \cdot \delta\boldsymbol{a}_3' \\ \boldsymbol{a}_2' \cdot \delta\boldsymbol{u}' + \boldsymbol{x}_0' \cdot \delta\boldsymbol{a}_2' \end{bmatrix} & \qquad \delta\boldsymbol{\alpha}' &= \begin{bmatrix} \delta\alpha_1' \\ \delta\alpha_2' \\ \delta\alpha_3' \end{bmatrix}
\end{aligned} \quad . \tag{40}$$

The virtual electric field $\delta\vec{\boldsymbol{E}}$ is defined as

$$\delta\vec{\boldsymbol{E}} = \bar{\boldsymbol{A}}\,\delta\bar{\vec{\boldsymbol{E}}} \qquad \text{with} \quad \delta\bar{\vec{\boldsymbol{E}}} = \begin{bmatrix}\delta\boldsymbol{\Phi} \\ \delta\boldsymbol{\Phi}'\end{bmatrix} \tag{41}$$

with

$$\delta\boldsymbol{\Phi} = [\delta c_1, \delta c_2, \delta c_3, \delta c_4, \delta c_5]^T \qquad \delta\boldsymbol{\Phi}' = [\delta c_1', \delta c_2', \delta c_3', \delta c_4', \delta c_5']^T \quad . \tag{42}$$

The internal virtual work that follows from Eq. (38) and is rewritten as

$$G_{int} = \int_{\mathcal{B}_0} \delta\boldsymbol{E}_b^T\,\boldsymbol{S}_b\,\mathrm{d}\,V - \int_{\mathcal{B}_0} \delta\vec{\boldsymbol{E}}^T\,\vec{\boldsymbol{D}}\,\mathrm{d}\,V = \int_S \delta\widehat{\boldsymbol{E}}^T\,\widehat{\boldsymbol{S}}\,\mathrm{d}\,S - \int_S \delta\bar{\vec{\boldsymbol{E}}}^T\,\bar{\vec{\boldsymbol{D}}}\,\mathrm{d}\,S \quad . \tag{43}$$

The work conjugate stress resultants $\widehat{\boldsymbol{S}}$ are obtained by integration over the cross section of the beam

$$\widehat{\boldsymbol{S}} = \int_\Omega \widehat{\boldsymbol{A}}^T\,\boldsymbol{S}_b\,\mathrm{d}\,A = \int_\Omega \begin{bmatrix} S_{11}\,\boldsymbol{e}_1 + S_{12}\,\boldsymbol{e}_2 + S_{13}\,\boldsymbol{e}_3 \\ \boldsymbol{W}_d\,(S_{11}\,\boldsymbol{e}_1 + S_{12}\,\boldsymbol{e}_2 + S_{13}\,\boldsymbol{e}_3) \\ \bar{\bar{\boldsymbol{\omega}}}_{,2}\;S_{12} + \bar{\bar{\boldsymbol{\omega}}}_{,3}\;S_{13} \\ \bar{\bar{\boldsymbol{\omega}}}\;S_{11} \end{bmatrix}_{[12\times1]} \mathrm{d}\,A \tag{44}$$

with $\boldsymbol{W}_d = \operatorname{skew} \boldsymbol{d}$ and the axial vector $\boldsymbol{d} = [0, \xi_2, \xi_3]^T$. The components of the vector $\widehat{\boldsymbol{S}}$ are defined as

$$\widehat{\boldsymbol{S}} = \begin{bmatrix} N & \text{normal force} \\ Q_2 \\ Q_3 & \text{shear forces} \\ M_1 & \text{torsional moment} \\ M_2 \\ M_3 & \text{bending moments} \\ N^{\bar{\omega}_1} & \text{bi-shear} \\ N^{\bar{\omega}_2} \\ N^{\bar{\omega}_3} & \text{bi-shear due to warping} \\ M^{\bar{\omega}_1} & \text{bi-moment} \\ M^{\bar{\omega}_2} \\ M^{\bar{\omega}_3} & \text{bi-moment due to warping} \end{bmatrix} \tag{45}$$

The work conjugate dielectric stress vector $\bar{\vec{\boldsymbol{D}}}$ is obtained similarly by integration over the cross section

$$\bar{\vec{\boldsymbol{D}}} = \int_\Omega \bar{\boldsymbol{A}}^T \vec{\boldsymbol{D}} \, \mathrm{d}\, A = \int_\Omega - \begin{bmatrix} \vec{D}_2 \, \boldsymbol{e}_2 + \vec{D}_3 \, \boldsymbol{e}_3 \\ -2 \, \xi_{p2} \, \vec{D}_2 \\ -2 \, \xi_{p3} \, \vec{D}_3 \\ \boldsymbol{\Phi} \, \vec{D}_1 \end{bmatrix}_{10\times 1} \mathrm{d}\, A \quad . \tag{46}$$

In contrast to $\widehat{\boldsymbol{S}}$, no descriptive interpretation of the components of $\bar{\vec{\boldsymbol{D}}}$ is established so far.

5.2 External virtual work

A detailed treatment of the mechanical part of the external virtual work is given in the publications of Gruttmann et al. [19, 21] and will not be discussed in this paper. For the description of the electrical part of the external virtual work the following consideration is proposed. The virtual electric potential is decomposed into the vectors $\delta\boldsymbol{\Phi}$ and $\bar{\boldsymbol{a}}$

$$\delta\phi = \bar{\boldsymbol{a}}(\xi_{p2}, \xi_{p3}) \cdot \delta\boldsymbol{\Phi}(S) \qquad \text{with} \quad \bar{\boldsymbol{a}} = \left[1 \quad \xi_{p2} \quad \xi_{p3} \quad \left(\tfrac{b_p^2}{4} - \xi_{p2}^2\right) \quad \left(\tfrac{h_p^2}{4} - \xi_{p3}^2\right)\right]^T \quad . \tag{47}$$

The integration over the surface $\partial_{\bar{\sigma}}\mathcal{B}_0$ of the beam is split into an integration over the beam coordinate S and a contour integral s over the cross section surface of the piezoelectric layer, see Fig. 3.

$$G_{ext}^{elc}(\boldsymbol{\Phi}, \delta\boldsymbol{\Phi}) = - \int_{\partial_{\bar{\sigma}}\mathcal{B}_0} \bar{\sigma}_0 \, \delta\phi \, \mathrm{d}\, A = - \int_S \delta\boldsymbol{\Phi}^T \underbrace{\left(\oint_s \bar{\sigma}_0 \, \bar{\boldsymbol{a}} \, \mathrm{d}\, s \right)}_{\bar{\boldsymbol{q}}_{\bar{\sigma}}} \mathrm{d}\, S \quad . \tag{48}$$

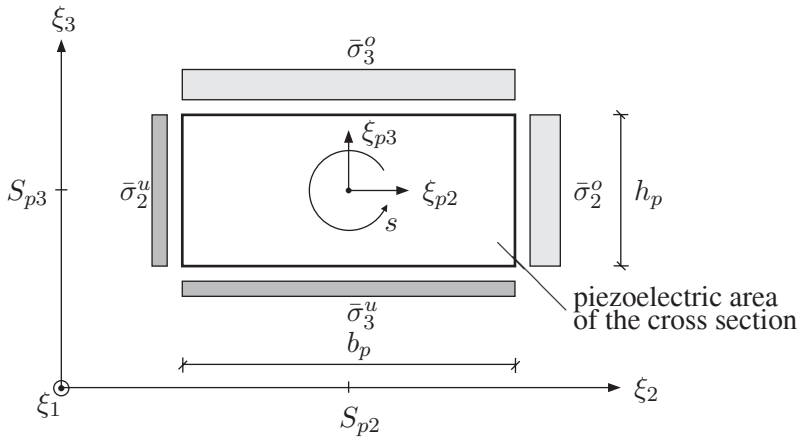

Figure 3: Definition of the surface load $\bar{\sigma}_i$.

Since we assume a rectangular shape of the piezoelectric material layer, the contour integral $\bar{\boldsymbol{q}}_{\bar{\sigma}}$ can be analytically determined as follows

$$\bar{\boldsymbol{q}}_{\bar{\sigma}} = \begin{bmatrix} (\bar{\sigma}_3^o + \bar{\sigma}_3^u)\, b_p & + & (\bar{\sigma}_2^o + \bar{\sigma}_2^u)\, h_p \\ 0 & + & \frac{1}{2}(\bar{\sigma}_2^o - \bar{\sigma}_2^u)\, h_p\, b_p \\ \frac{1}{2}(\bar{\sigma}_3^o - \bar{\sigma}_3^u)\, h_p\, b_p & + & 0 \\ \frac{1}{6}(\bar{\sigma}_3^o + \bar{\sigma}_3^u)\, b_p^3 & + & 0 \\ 0 & + & \frac{1}{6}(\bar{\sigma}_2^o + \bar{\sigma}_2^u)\, h_p^3 \end{bmatrix} \quad . \tag{49}$$

5.3 Linearization of the virtual work expressions

The weak form is solved approximately by employing the finite element method. Due to the nonlinearities the iterative solution strategy according to Newton-Raphson is utilized. This necessitates a further linearization of the weak form, which reads

$$\begin{aligned} \mathrm{Lin}[G(\boldsymbol{v} + \Delta\boldsymbol{v}, \delta\boldsymbol{v}, \boldsymbol{\Phi} + \Delta\boldsymbol{\Phi}, \delta\boldsymbol{\Phi})] &= G + [\mathrm{D}_v\, G \cdot\, \Delta\boldsymbol{v} + \mathrm{D}_\Phi\, G\, \Delta\boldsymbol{\Phi}] \\ \mathrm{D}_v\, G \cdot \Delta\boldsymbol{v} &= \frac{\mathrm{d}}{\mathrm{d}\,\alpha}[G(\boldsymbol{v} + \alpha\, \Delta\boldsymbol{v}, \delta\boldsymbol{v}, \boldsymbol{\Phi}, \delta\boldsymbol{\Phi})]_{\alpha=0} \\ \mathrm{D}_\phi\, G\, \Delta\boldsymbol{\Phi} &= \frac{\mathrm{d}}{\mathrm{d}\,\alpha}[G(\boldsymbol{v}, \delta\boldsymbol{v}, \phi + \alpha\, \Delta\boldsymbol{\Phi}, \delta\boldsymbol{\Phi})]_{\alpha=0} \quad . \end{aligned} \tag{50}$$

Applying Eq. (50) to the internal virtual work (43), its linearization is observed as

$$
\begin{aligned}
[\mathrm{D}_v\, G \cdot\ \Delta\boldsymbol{v} + \mathrm{D}_\Phi\, G\, \Delta\boldsymbol{\Phi}]_{int} = &\int_{\mathcal{B}_0} \delta\boldsymbol{E}_b^T (\tilde{\mathbb{C}}\, \Delta\boldsymbol{E}_b - \tilde{\mathrm{e}}\, \Delta\vec{\boldsymbol{E}})\ \mathrm{d}\,V \\
&- \int_{\mathcal{B}_0} \delta\vec{\boldsymbol{E}}^T (\tilde{\mathrm{e}}^T\, \Delta\boldsymbol{E}_b + \tilde{\boldsymbol{\epsilon}}\, \Delta\vec{\boldsymbol{E}} + \Delta\vec{\boldsymbol{P}}^i)\ \mathrm{d}\,V \\
&+ \int_{\mathcal{B}_0} \Delta\delta\boldsymbol{E}_b^T \boldsymbol{S}_b\ \mathrm{d}\,V - \int_{\mathcal{B}_0} \Delta\delta\vec{\boldsymbol{E}}^T \vec{\boldsymbol{D}}\ \mathrm{d}\,V
\end{aligned}
\quad . \tag{51}
$$

Here, the stresses $\boldsymbol{S}_b$ and the electric displacements $\vec{\boldsymbol{D}}$ are determined by the nonlinear material law (15). The linearized beam strains $\Delta\boldsymbol{E}_b = \widehat{\boldsymbol{A}}\, \Delta\hat{\boldsymbol{E}}$ with $\Delta\hat{\boldsymbol{E}} = [\Delta\boldsymbol{\varepsilon}, \Delta\boldsymbol{\kappa}, \Delta\boldsymbol{\alpha}, \Delta\boldsymbol{\alpha}']^T$ are formally obtained from Eq. (40) by replacing the operator δ by Δ. According to Sauer [47], the linearized virtual strains are given as

$$
\begin{aligned}
\Delta\delta\boldsymbol{\varepsilon} &= \begin{bmatrix} \delta\boldsymbol{u}' \cdot \Delta\boldsymbol{u}' \\ \delta\boldsymbol{a}_2 \cdot \Delta\boldsymbol{u}' + \delta\boldsymbol{u}' \cdot \Delta\boldsymbol{a}_2 + \boldsymbol{x}_0' \cdot \Delta\delta\boldsymbol{a}_2 \\ \delta\boldsymbol{a}_3 \cdot \Delta\boldsymbol{u}' + \delta\boldsymbol{u}' \cdot \Delta\boldsymbol{a}_3 + \boldsymbol{x}_0' \cdot \Delta\delta\boldsymbol{a}_3 \end{bmatrix} \\
\Delta\delta\boldsymbol{\kappa} &= \begin{bmatrix} \delta\boldsymbol{a}_2' \cdot \Delta\boldsymbol{a}_3 + \delta\boldsymbol{a}_3 \cdot \Delta\boldsymbol{a}_2' + \boldsymbol{a}_3 \cdot \Delta\delta\boldsymbol{a}_2' + \boldsymbol{a}_2' \cdot \Delta\delta\boldsymbol{a}_3 \\ \delta\boldsymbol{a}_3' \cdot \Delta\boldsymbol{u}' + \delta\boldsymbol{u}' \cdot \Delta\boldsymbol{a}_3' + \boldsymbol{x}_0' \cdot \Delta\delta\boldsymbol{a}_3' \\ \delta\boldsymbol{a}_2' \cdot \Delta\boldsymbol{u}' + \delta\boldsymbol{u}' \cdot \Delta\boldsymbol{a}_2' + \boldsymbol{x}_0' \cdot \Delta\delta\boldsymbol{a}_2' \end{bmatrix}
\end{aligned}
\quad . \tag{52}
$$

The linearized electric quantity $\Delta\bar{\vec{\boldsymbol{E}}} = \bar{\boldsymbol{A}}\, \Delta\bar{\vec{\boldsymbol{E}}}$ is defined as

$$
\Delta\bar{\vec{\boldsymbol{E}}} = \begin{bmatrix} \Delta\boldsymbol{\Phi} \\ \Delta\boldsymbol{\Phi}' \end{bmatrix} \qquad \text{with} \qquad \begin{aligned} \Delta\boldsymbol{\Phi} &= [\Delta c_1, \Delta c_2, \Delta c_3, \Delta c_4, \Delta c_5]^T \\ \Delta\boldsymbol{\Phi}' &= [\Delta c_1', \Delta c_2', \Delta c_3', \Delta c_4', \Delta c_5']^T \end{aligned} \quad , \tag{53}
$$

whereas the linearized virtual electric field is equal to zero, $\Delta\delta\bar{\vec{\boldsymbol{E}}} = \boldsymbol{0}$. With respect to Eqs. (23), (35) and integration through the cross section, the linearization of the inner virtual work reads

$$
\begin{aligned}
[\mathrm{D}_v\, G \cdot\ \Delta\boldsymbol{v} + \mathrm{D}_\Phi\, G\, \Delta\boldsymbol{\Phi}]_{int} = &\int_S (\delta\widehat{\boldsymbol{E}}^T\, \hat{\mathbb{D}}\, \Delta\widehat{\boldsymbol{E}} - \delta\widehat{\boldsymbol{E}}^T\, \hat{\bar{\mathbb{D}}}\, \Delta\bar{\vec{\boldsymbol{E}}})\ \mathrm{d}\,S \\
&+ \int_S (\delta\bar{\vec{\boldsymbol{E}}}^T\, \hat{\bar{\mathbb{D}}}^T\, \Delta\widehat{\boldsymbol{E}} + \delta\bar{\vec{\boldsymbol{E}}}\, \bar{\mathbb{D}}\, \Delta\bar{\vec{\boldsymbol{E}}})\ \mathrm{d}\,S + \int_S \Delta\delta\widehat{\boldsymbol{E}}^T\, \widehat{\boldsymbol{S}}\ \mathrm{d}\,S
\end{aligned}
\quad . \tag{54}
$$

The integration through the cross section yields the matrices

$$\hat{\mathbb{D}} = \int_{\Omega} \widehat{\boldsymbol{A}}^T \, \tilde{\mathbb{C}} \, \widehat{\boldsymbol{A}} \, \mathrm{d}\, A \qquad \hat{\bar{\mathbb{D}}} = \int_{\Omega} \widehat{\boldsymbol{A}}^T \, \tilde{\mathbb{e}} \, \bar{\boldsymbol{A}} \, \mathrm{d}\, A \qquad \bar{\mathbb{D}} = \int_{\Omega} \bar{\boldsymbol{A}}^T \, (\tilde{\boldsymbol{\epsilon}} + \boldsymbol{\epsilon}^{Pol}) \, \bar{\boldsymbol{A}} \, \mathrm{d}\, A \quad . \tag{55}$$

The quantity $\boldsymbol{\epsilon}^{Pol}$ occurs due to the material nonlinear constitutive Eq. (7). From the work expression it follows with a partial derivative of $\vec{\boldsymbol{P}}^i$ with respect to the electric field

$$\int_{\mathcal{B}_0} \delta\vec{\boldsymbol{E}}^T \, \frac{\partial \vec{\boldsymbol{P}}^i}{\partial \vec{\boldsymbol{E}}} \Delta\vec{\boldsymbol{E}} \, \mathrm{d}\, V = \int_{\mathcal{B}_0} \delta\vec{\boldsymbol{E}}^T \, \boldsymbol{\epsilon}^{Pol} \Delta\vec{\boldsymbol{E}} \, \mathrm{d}\, V \quad . \tag{56}$$

The second order tensor $\boldsymbol{\epsilon}^{Pol}$ is interpreted as the linearized part of electric permittivity.

For the linearization of the mechanical part of the external virtual work we refer to the publications of Sauer [47] and Gruttmann et al. [21]. For the problems discussed in this paper this quantity can be neglected. Since $\Delta\delta\boldsymbol{\Phi}$ is equal to zero, the linearization of the electrical part of the external virtual work is also equal to zero.

6 FINITE ELEMENT APPROXIMATION

According to the isoparametric concept, the following independent variables are approximated using linear shape functions $N_1(\xi) = \frac{1}{2}(1-\xi)$ and $N_2(\xi) = \frac{1}{2}(1+\xi)$ with $-1 \leq \xi \leq 1$

$$\begin{aligned} \boldsymbol{X}_0^h &= \sum_{I=1}^{2} \boldsymbol{X}_{0\,I} \, N_I(\xi) & \boldsymbol{x}_0^h &= \sum_{I=1}^{2} (\boldsymbol{X}_{0\,I} + \boldsymbol{u}_I) \, N_I(\xi) \\ \boldsymbol{\alpha}^h &= \sum_{I=1}^{2} \boldsymbol{\alpha}_I \, N_I(\xi) & \boldsymbol{\Phi}^h &= \sum_{I=1}^{2} \boldsymbol{\Phi}_I \, N_I(\xi) \quad . \end{aligned} \tag{57}$$

The index h characterizes the approximated quantities and the subscript I denotes the node number. The basis systems $\boldsymbol{A}_m$ and $\boldsymbol{a}_m$ are interpolated using the same shape functions

$$\boldsymbol{A}_m^h = \sum_{I=1}^{2} \boldsymbol{A}_{m\,I} \, N_I(\xi) \qquad \boldsymbol{a}_m^h = \sum_{I=1}^{2} \boldsymbol{a}_{m\,I} \, N_I(\xi) \quad . \tag{58}$$

The base vectors $\boldsymbol{A}_m$ of the reference configuration are obtained from geometrical considerations of the undeformed finite element mesh. The base vector $\boldsymbol{a}_m$ of the current configuration follow from Eq. (17). Thus, the rotation tensor $\boldsymbol{R}_I$ must be determined using the Rodriguez

formula. With three independent parameters arranged in the pseudovector $\boldsymbol{\omega}$, the Rodriguez formula is given as

$$\boldsymbol{R}_I = \boldsymbol{a}_{m\,I} \otimes \boldsymbol{e}_m = \mathbf{1} + \frac{\sin\omega_I}{\omega_I}\,\boldsymbol{\Omega}_I + \frac{1-\cos\omega_I}{\omega_I^2}\,\boldsymbol{\Omega}_I^2 \quad . \tag{59}$$

The norm $\omega_I = \|\boldsymbol{\omega}_I\| = \sqrt{\omega_{1\,I}^2 + \omega_{2\,I}^2 + \omega_{3\,I}^2}$ of the pseudo vector corresponds to the magnitude of the rotation. For the skew symmetric tensor $\boldsymbol{\Omega}_I$ the relation $\boldsymbol{\Omega}_I\,\boldsymbol{h} = \boldsymbol{\omega}_I \times \boldsymbol{h}$ for all vectors $\boldsymbol{h} \in R^3$ is valid

$$\boldsymbol{\Omega}_I = \begin{bmatrix} 0 & -\omega_{3\,I} & \omega_{2\,I} \\ \omega_{3\,I} & 0 & -\omega_{1\,I} \\ -\omega_{2\,I} & \omega_{1\,I} & 0 \end{bmatrix} \qquad \text{with} \qquad \boldsymbol{\omega}_I = \begin{bmatrix} \omega_{1\,I} \\ \omega_{2\,I} \\ \omega_{3\,I} \end{bmatrix} \quad . \tag{60}$$

The interpolation of the virtual quantities and the associated linearizations are given as

$$\begin{aligned} \delta\boldsymbol{u}^h &= \sum_{I=1}^{2} \delta\boldsymbol{u}_I\,N_I(\xi) & \delta\boldsymbol{\alpha}^h &= \sum_{I=1}^{2} \delta\boldsymbol{\alpha}_I\,N_I(\xi) & \delta\boldsymbol{\Phi}^h &= \sum_{I=1}^{2} \delta\boldsymbol{\Phi}_I\,N_I(\xi) \\ \delta\boldsymbol{a}_m^h &= \sum_{I=1}^{2} \delta\boldsymbol{a}_{m\,I}\,N_I(\xi) & \Delta\delta\boldsymbol{a}_m^h &= \sum_{I=1}^{2} \Delta\delta\boldsymbol{a}_{m\,I}\,N_I(\xi) \end{aligned} \tag{61}$$

For the linearization of the virtual basis vectors $\Delta\delta\boldsymbol{a}_{m\,I}$ see Gruttmann et al. [21] and Sauer [47]. The definition of the virtual basis vectors $\delta\boldsymbol{a}_{m\,I}$ reads

$$\delta\boldsymbol{a}_{m\,I} = \delta\boldsymbol{R}_I\,\boldsymbol{R}_I^T\,\boldsymbol{a}_{m\,I} = \delta\boldsymbol{w}_I \times \boldsymbol{a}_{m\,I} = \boldsymbol{W}_{m\,I}^T\,\delta\boldsymbol{w}_I \tag{62}$$

with $\boldsymbol{W}_{m\,I} = \text{skew}(\boldsymbol{a}_{m\,I})^T$. The scalar product of the linearized, virtual basis systems and an arbitrary vector $\boldsymbol{h}$ is approximated by

$$\boldsymbol{h} \cdot \Delta\delta\boldsymbol{a}_m^h = \sum_{I=1}^{2} N_I\,\delta\boldsymbol{w}_I \cdot \boldsymbol{M}(\boldsymbol{a}_{m\,I}, \boldsymbol{h})\,\Delta\boldsymbol{w}_I \quad . \tag{63}$$

Here, the matrix $\boldsymbol{M}(\boldsymbol{a}_{m\,I}, \boldsymbol{h})$ is defined as

$$\begin{aligned} \boldsymbol{M}(\boldsymbol{a}_{m\,I}, \boldsymbol{h}) = &\frac{1}{2}(\boldsymbol{a}_{m\,I} \otimes \boldsymbol{h} + \boldsymbol{h} \otimes \boldsymbol{a}_{m\,I}) - (\boldsymbol{a}_{m\,I} \cdot \boldsymbol{h})\,\mathbf{1} \\ &- \hat{c}_3 \left[\frac{1}{2}(\boldsymbol{b}_{m\,I} \otimes \boldsymbol{\omega}_I + \boldsymbol{\omega}_I \otimes \boldsymbol{b}_{m\,I}) - (\boldsymbol{b}_{m\,I} \cdot \boldsymbol{\omega}_I)\,\mathbf{1}\right] \\ &+ \hat{c}_4(\boldsymbol{b}_{m\,I} \cdot \boldsymbol{\omega}_I)\,\boldsymbol{\Omega}_I^2 \end{aligned} \tag{64}$$

and the constants

$$\hat{c}_3 = \frac{2\cos\omega_I + \omega_I \sin\omega_I - 2}{w_I^2\,(\cos\omega_I - 1)} \quad \text{and} \quad \hat{c}_4 = \frac{4\cos\omega_I + \omega_I \sin\omega_I + \omega_I^2 - 4}{2\,\omega_I^4\,(cos\omega_I - 1)}\,. \tag{65}$$

The approximation of the virtual beam strains $\delta\widehat{\boldsymbol{E}}$ follows from virtual beam kinematics $\delta\boldsymbol{v}_I = [\delta\boldsymbol{u}_I, \delta\boldsymbol{w}_I, \delta\boldsymbol{\alpha}_I]^T$ and the mechanical $\hat{\boldsymbol{B}}_I$ matrix

$$\delta\widehat{\boldsymbol{E}}^h = \sum_{I=1}^{2} \hat{\boldsymbol{B}}_I\, \delta\boldsymbol{v}_I, \qquad \text{with} \quad \hat{\boldsymbol{B}}_I = \begin{bmatrix} \boldsymbol{x}_0^T\, N_I' & \boldsymbol{0} & \boldsymbol{0} \\ \boldsymbol{a}_2^T\, N_I' & \boldsymbol{b}_{2\,I}^T(\boldsymbol{x}_0')\, N_I & \boldsymbol{0} \\ \boldsymbol{a}_3^T\, N_I' & \boldsymbol{b}_{3\,I}^T(\boldsymbol{x}_0')\, N_I & \boldsymbol{0} \\ \boldsymbol{0} & \boldsymbol{b}_{2\,I}^T(\boldsymbol{a}_3)\, N_I' & \boldsymbol{0} \\ \boldsymbol{a}_3'^T\, N_I' & \boldsymbol{b}_{3\,I}'^T(\boldsymbol{x}_0')\, N_I + \boldsymbol{b}_{3\,I}^T(\boldsymbol{x}_0')\, N_I' & \boldsymbol{0} \\ \boldsymbol{a}_2'^T\, N_I' & \boldsymbol{b}_{2\,I}'^T(\boldsymbol{x}_0')\, N_I + \boldsymbol{b}_{2\,I}^T(\boldsymbol{x}_0')\, N_I' & \boldsymbol{0} \\ \boldsymbol{0} & \boldsymbol{0} & \boldsymbol{1}_{3\times3}\, N_I \\ \boldsymbol{0} & \boldsymbol{0} & \boldsymbol{1}_{3\times3}\, N_I' \end{bmatrix} \tag{66}$$

Here, the vector $\boldsymbol{b}_{m\,I}$ and its derivative with respect the beam coordinate S are defined as

$$\boldsymbol{b}_{m\,I}(\boldsymbol{h}) = \boldsymbol{a}_{m\,I} \times \boldsymbol{h} \qquad\qquad \boldsymbol{b}_{m\,I}'(\boldsymbol{h}) = \boldsymbol{a}_{m\,I}' \times \boldsymbol{h} \quad . \tag{67}$$

For the approximation of the virtual electric field $\delta\bar{\vec{\boldsymbol{E}}}$, the virtual electrical quantity $\delta\boldsymbol{\Phi}_I$ and the electrical $\bar{\boldsymbol{B}}_I$ matrix are used

$$\delta\bar{\vec{\boldsymbol{E}}}^h = \sum_{I=1}^{2} \bar{\boldsymbol{B}}_I\, \delta\boldsymbol{\Phi}_I \qquad \text{with} \quad \bar{\boldsymbol{B}}_I = \begin{bmatrix} N_I\, \boldsymbol{1}_{5\times5} \\ N_I'\, \boldsymbol{1}_{5\times5} \end{bmatrix}_{[10\times5]} \quad . \tag{68}$$

Considering the former approximations in the weak form, the linearized boundary value problem of Eq. (51) reads

$$\mathrm{Lin}[G(\boldsymbol{v}^h, \delta\boldsymbol{v}^h, \boldsymbol{\Phi}^h, \delta\boldsymbol{\Phi}^h)] = \bigcup_{e=1}^{numel} \sum_{I=1}^{2} \sum_{K=1}^{2} \begin{bmatrix} \delta\boldsymbol{v}_I \\ \delta\boldsymbol{\Phi}_I \end{bmatrix}^T \left(\begin{bmatrix} \hat{\boldsymbol{f}}_I \\ \bar{\boldsymbol{f}}_I \end{bmatrix} + \begin{bmatrix} \hat{\boldsymbol{K}}_{T\,IK} & -\hat{\bar{\boldsymbol{K}}}_{T\,IK} \\ \hat{\bar{\boldsymbol{K}}}_{T\,IK}^T & \bar{\boldsymbol{K}}_{T\,IK} \end{bmatrix} \begin{bmatrix} \Delta\boldsymbol{v}_K \\ \Delta\boldsymbol{\Phi}_K \end{bmatrix} \right) \tag{69}$$

The vectors $\hat{\boldsymbol{f}}_I$ and $\bar{\boldsymbol{f}}_I$ represent the mechanical and electrical loading on element level

$$\hat{\boldsymbol{f}}_I^e = \int_S \hat{\boldsymbol{B}}_I^T\, \widehat{\boldsymbol{S}} - N_I\, \hat{\boldsymbol{q}}\, \mathrm{d}\,S \qquad\qquad \bar{\boldsymbol{f}}_I^e = \int_S \bar{\boldsymbol{B}}_I^T\, \bar{\vec{\boldsymbol{D}}} + N_I\, \bar{\boldsymbol{q}}_s\, \mathrm{d}\,S \quad . \tag{70}$$

The tangential stiffness matrix is divided into a mechanical, a mixed and an electrical submatrix which are defined as

$$\hat{\boldsymbol{K}}_{T\,IK} = \int_S \left(\hat{\boldsymbol{B}}_I^T\, \hat{\mathbb{D}}\, \hat{\boldsymbol{B}}_K + \hat{\boldsymbol{G}}_{IK} + \hat{\boldsymbol{P}}_{IK} \right) \mathrm{d}\,S \tag{71}$$

$$\hat{\bar{\boldsymbol{K}}}_{T\,IK} = \int_S \hat{\boldsymbol{B}}_I^T\, \hat{\bar{\mathbb{D}}}\, \bar{\boldsymbol{B}}_K\, \mathrm{d}\,S \qquad\qquad \bar{\boldsymbol{K}}_{T\,IK} = \int_S \bar{\boldsymbol{B}}_I^T\, \bar{\mathbb{D}}\, \bar{\boldsymbol{B}}_K\, \mathrm{d}\,S \tag{72}$$

In the mechanical part $\hat{\boldsymbol{K}}_{T\,IK}$ the additional stiffness components $\hat{\boldsymbol{G}}_{IK}$ and $\hat{\boldsymbol{P}}_{IK}$ arise due to linearization of the internal and external virtual work. The so called geometrical stiffness matrix describes the correlation between the stress resultants $\hat{\boldsymbol{S}}$ and the quantities $\boldsymbol{x}_0'$, $\boldsymbol{a}_m$ and $\boldsymbol{a}_m'$. It is defined as

$$\hat{\boldsymbol{G}}_{IK} = \begin{bmatrix} \boldsymbol{G}_{IK}^{uu} & \boldsymbol{G}_{IK}^{uw} & \boldsymbol{0} \\ \boldsymbol{G}_{IK}^{wu} & \boldsymbol{G}_{IK}^{ww} & \boldsymbol{0} \\ \boldsymbol{0} & \boldsymbol{0} & \boldsymbol{0} \end{bmatrix}_{[9\times 9]} \tag{73}$$

with the following submatrices

$$\begin{aligned}
\boldsymbol{G}_{IK}^{uu} &= N_I'\, N_K'\, \boldsymbol{1}_{3\times 3}\, N^1 \\
\boldsymbol{G}_{IK}^{uw} &= N_I'\, N_K\, \hat{\boldsymbol{W}}_{q\,K}^{T} + N_I'\, N_K'\, \hat{\boldsymbol{W}}_{m\,K}^{T} + N_I'\, N_K\, \hat{\boldsymbol{W}}_{m\,K}^{\prime\,T} \\
\boldsymbol{G}_{IK}^{wu} &= N_I\, N_K'\, \hat{\boldsymbol{W}}_{q\,I} + N_I'\, N_K'\, \hat{\boldsymbol{W}}_{m\,I} + N_I\, N_K'\, \hat{\boldsymbol{W}}_{m\,I}^{\prime} \\
\boldsymbol{G}_{IK}^{ww} &= N_I'\, N_K\, \boldsymbol{M}_{IK}^{23} + N_I\, N_K'\, \boldsymbol{M}_{IK}^{32} + N_I\, N_K\, \boldsymbol{M}_{IK}' + (N_I\, \boldsymbol{M}_{q\,I} + N_I'\, \boldsymbol{M}_{m\,I})\, \delta_{IK} \quad .
\end{aligned} \tag{74}$$

The expressions in Eq. (74) are given as

$$\begin{aligned}
\hat{\boldsymbol{W}}_{q\,I}^{T} &= \boldsymbol{W}_{2\,I}\, Q_2 + \boldsymbol{W}_{3\,I}\, Q_3 \,, & \boldsymbol{M}_{IK}^{23} &= \boldsymbol{W}_{2\,I}\, \boldsymbol{W}_{3\,K}^{T}\, M_1 \\
\hat{\boldsymbol{W}}_{m\,I}^{T} &= \boldsymbol{W}_{3\,I}\, M_2 + \boldsymbol{W}_{2\,I}\, M_3 \,, & \boldsymbol{M}_{IK}^{32} &= \boldsymbol{W}_{3\,I}\, \boldsymbol{W}_{2\,K}^{T}\, M_1 \\
\hat{\boldsymbol{W}}_{m\,I}^{\prime\,T} &= \boldsymbol{W}_{3\,I}'\, M_2 + \boldsymbol{W}_{2\,I}'\, M_3 \,, & \boldsymbol{M}_{IK}' &= (\boldsymbol{W}_{2\,I}'\, \boldsymbol{W}_{3\,K}^{T} + \boldsymbol{W}_{3\,I}\, \boldsymbol{W}_{2\,K}^{\prime\,T})\, M_1
\end{aligned} \tag{75}$$

and

$$\begin{aligned}
\boldsymbol{M}_{q\,I} &= \boldsymbol{M}_{2\,I}(\boldsymbol{x}_0')\, Q_2 + \boldsymbol{M}_{3\,I}(\boldsymbol{x}_0')\, Q_3 + \boldsymbol{M}_{3\,I}(\boldsymbol{a}_2')\, M_1 \\
\boldsymbol{M}_{m\,I} &= \boldsymbol{M}_{2\,I}(\boldsymbol{a}_3)\, M_1 + \boldsymbol{M}_{3\,I}(\boldsymbol{x}_0')\, M_2 + \boldsymbol{M}_{2\,I}(\boldsymbol{x}_0')\, M_3 \,,
\end{aligned} \tag{76}$$

using the abbreviations $\boldsymbol{W}_{i\,I} = \mathrm{skew}(\boldsymbol{a}_{i\,I})^T$,$\boldsymbol{W}_{i\,I}' = \mathrm{skew}(\boldsymbol{a}_{i\,I}')^T$ and $\boldsymbol{M}_{i\,I}(\boldsymbol{h}) = \boldsymbol{M}(\boldsymbol{a}_{i\,I}, \boldsymbol{h})$. Since the matrix $\hat{\boldsymbol{P}}_{IK}$ affects only the mechanical part of the beam formulation and is not relevant for the subsequent numerical examples, we refer to Gruttmann et al. [21] for a detailed discussion.

7 NUMERICAL EXAMPLES

The developed finite element formulation is implemented in an enhanced version of the general-purpose finite element program FEAP documented in Ref. [55]. In the first example, we discuss the nonlinear material model and demonstrate its applicability to ferroelectric hysteresis phenomena. The extended beam formulation is analyzed in the following two examples. Here, a special emphasis is on the influence of the introduced warping functions.

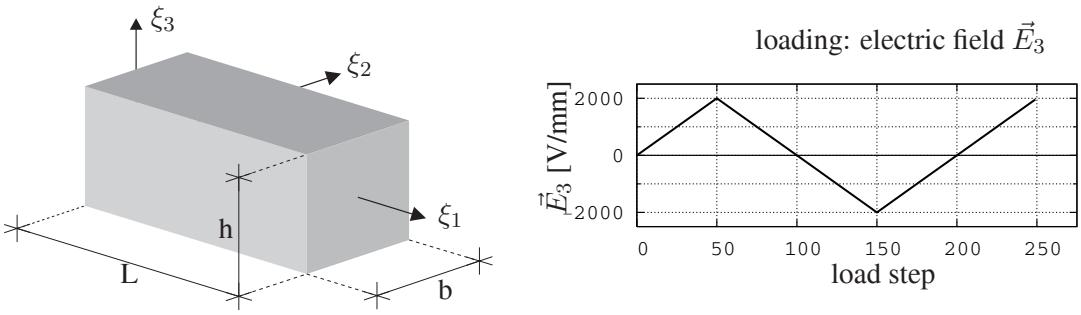

Figure 4: Configuration and loading of the piezoelectric specimen.

This is followed by an example for a piezoelectric buckling problem that may be utilized for switching devices. In the last example, we demonstrate the capability of the presented formulation on a typical three-dimensional piezoelectric structure.

For a better visualization of the numerical results the beam model is displayed as a three dimensional structure which is generated in a post processing operation using the data of the beam element and the corresponding cross section definition.

7.1 Ferroelectric Hysteresis

To illustrate the applicability of the Preisach model to ferroelectric hysteresis phenomena, we use a simple example which has already been discussed by Kamlah [26]. The geometry of the specimen is given in Fig. 4 with $L = 1.0\ mm$ and $b = h = 0.5\ mm$. It consists of a piezoelectric ceramic material which is completely depolarized in the initial state. Instead of experimental data, we use the following analytical weighting function in the Preisach model.

$$\mu(\alpha, \beta) = c\, e^{[-f_\alpha\,(\alpha+\beta-y_\alpha-y_\beta)^2 - f_\beta\,(\beta-\alpha+y_\alpha-y_\beta)^2]} \quad . \tag{77}$$

This function is based on the one proposed by Barker [5]. The parameters in Eq. (77) are given as follows: $c = 25$, $f_\alpha = f_\beta = 12.5$, $y_\alpha = -y_\beta = 0.5$. According to [26], we specify the coercive field strength $\vec{E}^c = 1 \cdot 10^6\ V/m$, the saturation polarization $\vec{P}^{sat} = 0.300\ C/m^2$ and the irreversible strain $E^{sat} = 0.002$. The linear parameters for the completely polarized material are listed in Appendix A.1. The specimen is loaded with a quasi static electric field in ξ_3-direction as shown in Fig. 4. Thus, the vector $\boldsymbol{e}^P$ is determined as $\boldsymbol{e}^P = [0, 0, 1]^T$. Since the analyzed problem is very simple, it is sufficient to use one beam element for the discretization in ξ_1-direction an one element to model the cross section.

The results from the finite element computation are given in Fig. 5. The high electrical loading causes the typical ferroelectric hysteresis effects. The dielectric hysteresis as well as the butterfly hysteresis show a good agreement compared to the results of Kamlah [26]. The deviations can be explained by the usage of different functions to determine the irreversible

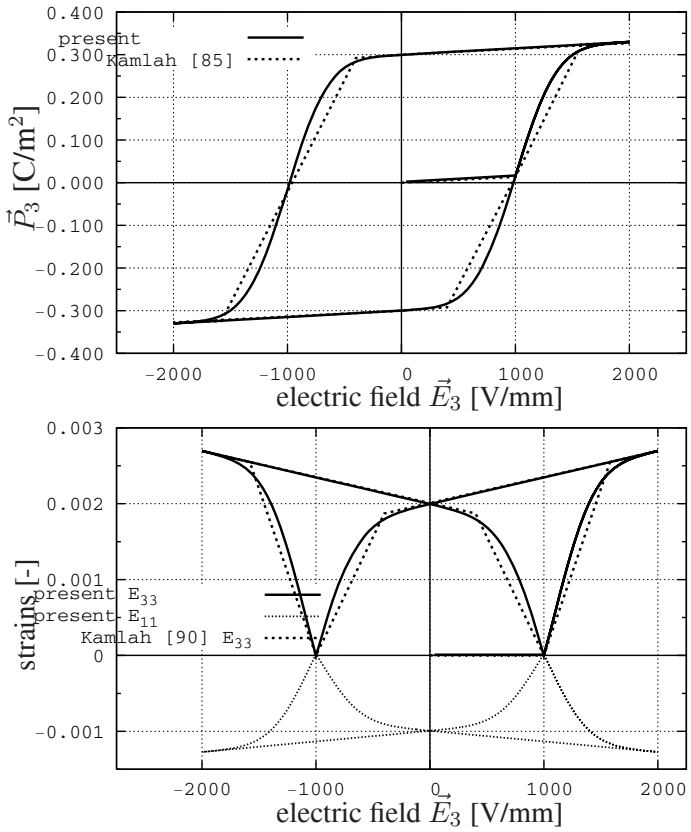

Figure 5: Resulting dielectric and butterfly hysteresis.

field quantities. The butterfly hysteresis in Fig. 5 corresponds to the resulting strain components E_{11} and E_{33}. It is noted that only the strain E_{11} follows directly from the beam formulation. In order to compare the results with the data from literature, the strain E_{33} is computed under consideration of the nonlinear material law given in Equation $(7)_1$.

An important criterion for the quality of a nonlinear material model is its convergence to the state of equilibrium. Therefore, the convergence of the residual norm is analyzed for two defined load steps. In case one, we consider an increasing electric field from 600 to $640\ V/mm$ which corresponds to the load step number 230 in Fig. 4. At this load level, the nonlinear hysteresis effects are just at the beginning. In the second case, we analyze the load step number 124 from -960 to $-1000\ V/mm$. Here, the gradient of the irreversible polarization between two load increments is maximal. The residual norm is summarized for each iteration step in Tab. 1. The presented nonlinear material model shows an excellent convergence for both cases. This is an essential feature in order to analyze larger problems in an efficient manner which will be shown in the later examples.

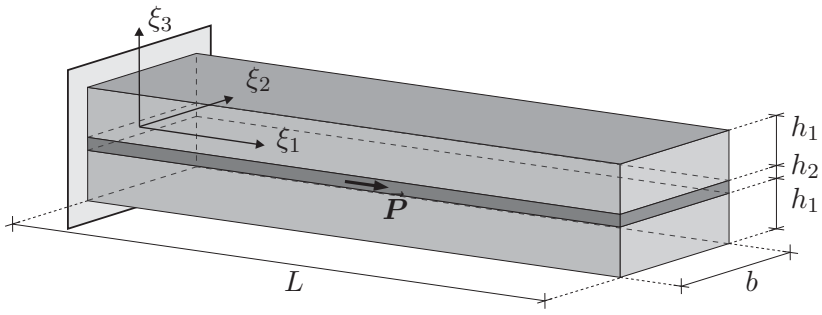

Figure 6: Shear actuator with geometrical data.

7.2 Shear actuator

In this example the shear actuator configuration proposed by Sun & Zhang [53] is discussed. Several publications can be found, in which this actuator is analyzed analytically [1, 61], numerically [8, 9] or experimentally in a modified configuration [4].

The actuator complies with a clamped beam that is made of three layers. The geometry of the system is given in Fig. 6. Both outer layer consist of aluminum with an elastic modulus of $70.3\ GPa$ and Poisson's ratio of 0.345. The middle layer is made of PZT-5H piezoelectric ceramic which is polarized in ξ_1-direction. The material data are given in appendix A.2. The piezoelectric layer is loaded with an electric potential of $20\ V$ in ξ_3-direction. For the numerical computation the structure is discretisized with 20 beam elements. All mechanical and the electrical degree of freedom c_1 are fixed at the clamping at $\xi_1 = 0$. The given electric potential corresponds to an electric field $\vec{E}_3$ of $1 \cdot 10^4\ V/m$. Within the beam formulation, this loading is realized by a prescribed electric degree of freedom c_3 with a value of $-1 \cdot 10^4\ V/m$ on all nodes.

The discretization of the cross section is illustrated in Fig. 7. For each layer 12×6 elements are used. Since the electric field is applied perpendicular to the poling direction of the PZT-5H layer, the piezoelectrically induced shear deformation has to be considered in an appropriate manner. For this, the unit warping of the cross section due to a shear deformation of the piezoelectric layer is computed. The corresponding warping function is shown in

Iteration	Case 1: load step number 230 $\vec{E}_3$ from 600 to 640 [V/mm]	Case 2: load step number 124 $\vec{E}_3$ from -960 to -1000 [V/mm]
1	$4.8 \cdot 10^{0}$	$2.7 \cdot 10^{1}$
2	$8.5 \cdot 10^{1}$	$2.2 \cdot 10^{2}$
3	$5.4 \cdot 10^{-3}$	$3.7 \cdot 10^{-2}$
4	$3.2 \cdot 10^{-11}$	$1.2 \cdot 10^{-9}$

Table 1: Residual norm for each iteration step for both load steps.

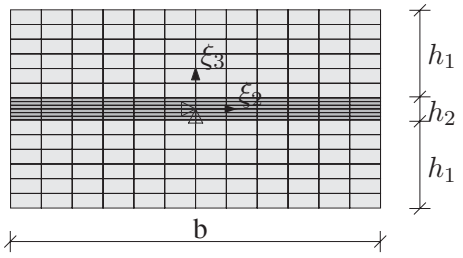

Figure 7: Geometrical data and finite element discretization of the cross section.

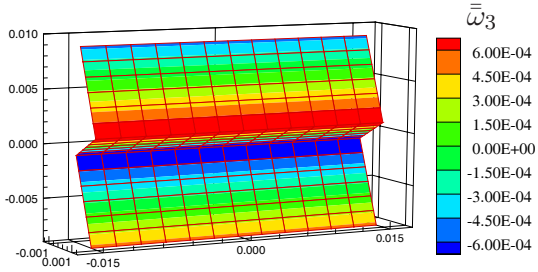

Figure 8: Warping function due to piezoelectrically induced shear deformation.

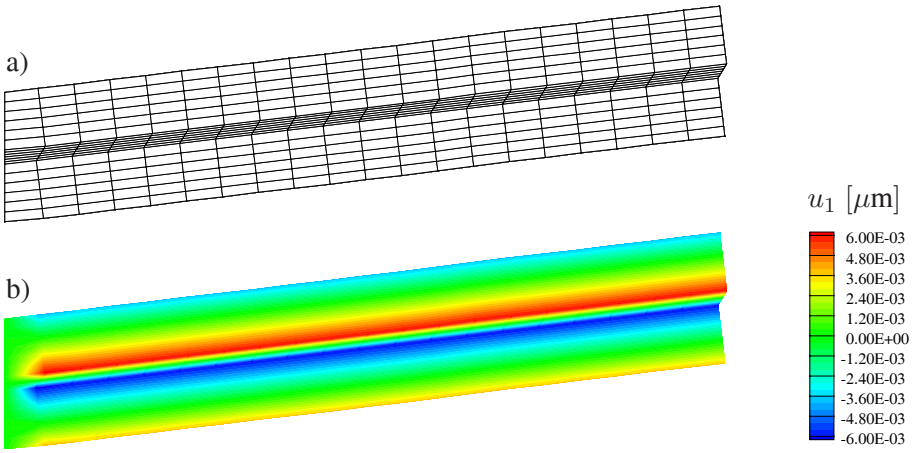

Figure 9: a) Deformed beam structure. b) Contour plot of the displacement u_1. Scaling factor $1 \cdot 10^5$

Fig. 8. The deformed beam configuration and the displacements u_1 are illustrated in Fig. 9. The deflection u_3 which is linear in ξ_1-direction is typical for this kind of actuators.

The displacements u_3 are now compared with the numerical results according to Benjeddou et al. [8] and the analytical solution of Zhang & Sun [61]. All results agree very well, as shown in Fig. 10. The references [8] and [61] use a modeling technique with three coupled beam layers. The layerwise modeling can be avoided in the presented beam model since the extended description of the cross section including warping is considered in the formulation. The importance of this concept becomes clear, if the warping functions are neglected in the numerical computation. In this case, the resulting displacements u_3 are underestimated by approximately the factor 1.5, see Fig. 10. Finally, the displacements are compared with the results of a finite element computation using an eight node brick element, see Linnemann & Klinkel [32]. For this, each layer of the shear actuator is discretisized with $20 \times 6 \times 12$ brick elements. Again, the displacements do agree very well as can be seen in Fig. 10.

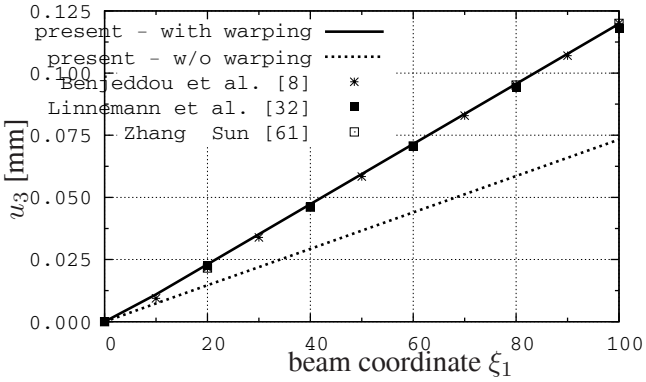

Figure 10: Displacement u_3 of the beam axis.

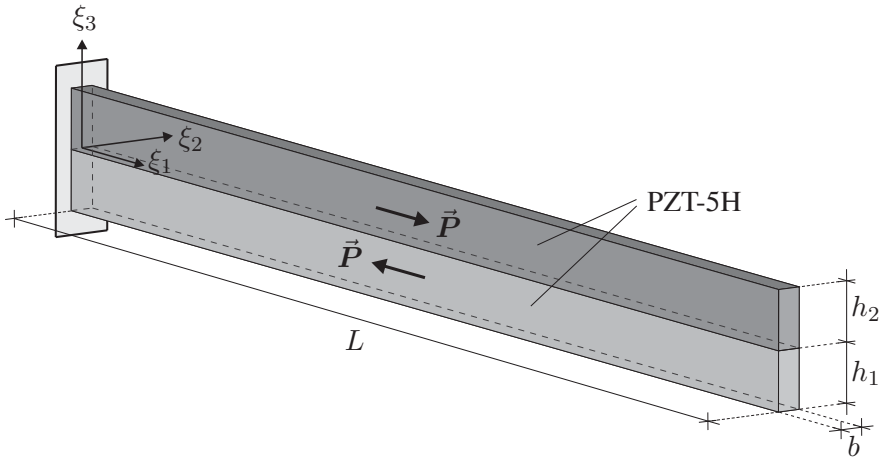

Figure 11: Configuration of the torsional actuator.

7.3 Torsional actuator

In this example the shear deformation effect is used to achieve a torsional deformation of the clamped beam configuration shown in Fig. 11 with $L = 100\ mm$, $b = 2\ mm$ and $h_1 = h_2 = 5\ mm$. It is made of two piezoelectric PZT-5H layer which are poled both in ξ_1-direction but with opposite sign. The material parameters of the upper layer are are given in Appendix A.2. The beam surface at $\xi_2 = -b/2$ is loaded with an electric potential of $1000\ V$. This corresponds to an electric field $\vec{E}_2$ of $-5 \cdot 10^5\ V/m$. Since the loading is perpendicular to the poling direction, a shear deformation will be induced in $-\xi_2$-direction for the upper layer and in ξ_2-direction for the lower layer. This opposite shear deformation will cause a torsional deformation of the beam structure since the geometric compatibility at $\xi_3 = 0$ must be fulfilled. For the numerical analysis, the structure is discretisized with 20 beam elements. The loading is realized with a prescribed degree of freedom $c_2 = 5 \cdot 10^5$ for

all nodes.

To account for the warping effects, the cross section is discretisized with 10×10 elements for each layer as depicted in Fig. 12. Furthermore, this Figure illustrates the warping functions $\bar{\bar{\omega}}_1$ and $\bar{\bar{\omega}}_2$ which correspond to a unit torque of the beam axis and a unit shear deformation due to the prescribed loading, respectively. It is obvious that the shear induced warping function is very similar to the well known warping function due to torsion. In a more detailed examination one significant difference arises. In contrast to the torsional induced warping function, the shear induced warping function is nearly constant in ξ_3-direction in the upper und lower areas of the cross section. Nearby the layer boundary this constant distribution cannot be preserved due to the geometrical compatibility constraint at $\xi_3 = 0$.

The deformed structure of the numerical computation is shown in Fig. 13. The twisted beam axis and the warping of the cross section can be seen clearly. Since this example is not discussed in other publications so far, the results have to be verified with an other numerical model. For this reason, we use the results of a finite element computation with piezoelectric brick elements according to Linnemann & Klinkel [32] and compare the displacement components of point A which is defined in Fig. 13. To determine the displacement components u_1, u_2 and u_3, it is necessary to consider the torsion φ_1 and the warping $\alpha_1 \, \bar{\bar{\omega}}_1(\xi_2^A, \xi_3^A)$ and $\alpha_2 \, \bar{\bar{\omega}}_2(\xi_3^A, \xi_3^A)$. The values are given as $\varphi_1 = 4.3689 \times 10^{-3} \; rad$, $\alpha_1 = 4.2117 \times 10^{-2}$, $\alpha_2 = -3.6956 \times 10^{-4}$. To provide a comparable discretization, the beam structure is divided into 20 brick elements in ξ_1-direction and in 10 elements in ξ_2- and ξ_3-direction for each layer. The results of both numerical computations are summarized in Tab. 2 and show a very good agreement. This example illustrates the high efficiency of the presented beam formulation. The displacements are comparable to the ones obtained from the brick element

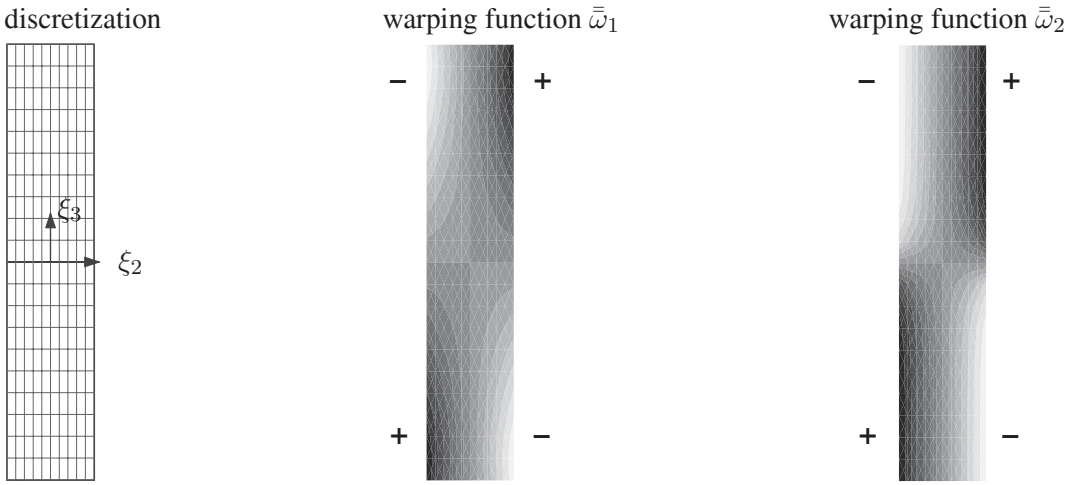

Figure 12: Discretization of the cross section with 10×10 elements for each layer and qualitative illustration of the warping functions $\bar{\bar{\omega}}_1$ and $\bar{\bar{\omega}}_2$. The algebraic signs correspond to the out of plane direction of the warping function.

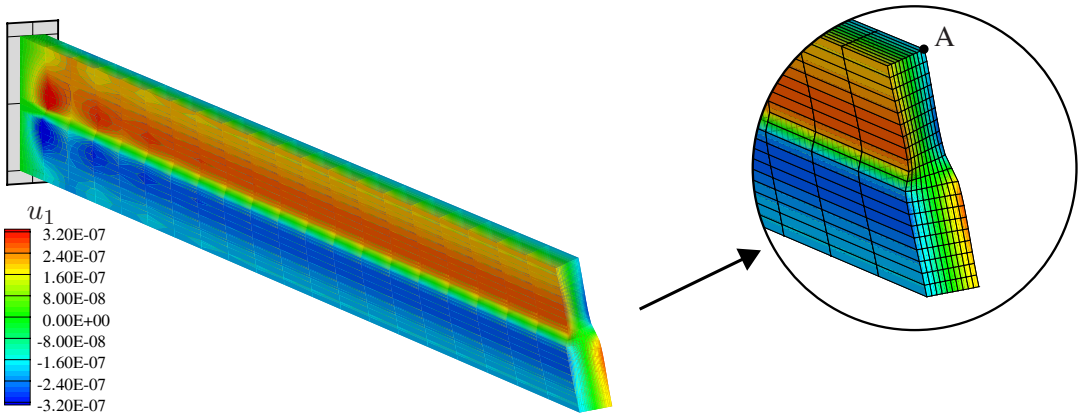

Figure 13: Deformed beam structure and detail view. The displacements u_2 und u_3 are scaled by the factor 50 the displacement u_1 by the factor 2000.

formulation, but with much less numerical effort.

displacement	present formulation [mm]	brick elements [32] [mm]	deviation of present formulation in [%]
u_1	-2.029×10^{-7}	-2.022×10^{-7}	0.35
u_2	-2.184×10^{-5}	-2.180×10^{-5}	0.18
u_3	4.369×10^{-6}	4.281×10^{-6}	2.06

Table 2: Comparison of the displacement components of point A located at (100,1,5).

7.4 Piezoelectric switch

This example analyzes the applicability of piezoelectric switching devices. Since the resulting deformations are small, these components are commonly used in microelectromechanical systems (MEMS), see e.g. [18, 48, 51]. Here, we use the buckling of a slender beam structure to model a piezoelectric switch. The displacement perpendicular to the beam axis is used to realize the on- and off-state of the device. The configuration of this switch is illustrated in Fig. 14. It consists of a silicon layer with an additional PZT-4 layer and a platinum electrode. An electric voltage is applied in ξ_3-direction that causes a positive straining of the PZT-4 material in ξ_1-direction. Since the corresponding elongation is constrained due to the boundary conditions, the prescribed loading will cause a compression stress in the piezoelectric material. The layered composition of the beam structure provides a small eccentricity and imposes a bending moment M_2 about the ξ_2-axis due to the loading.

The length of the analyzed structure varies between 500 and 700 μm, the total height is 2.05 μm. The width and the height of each layer are given in Tab. 3. Consequently, the dimensions

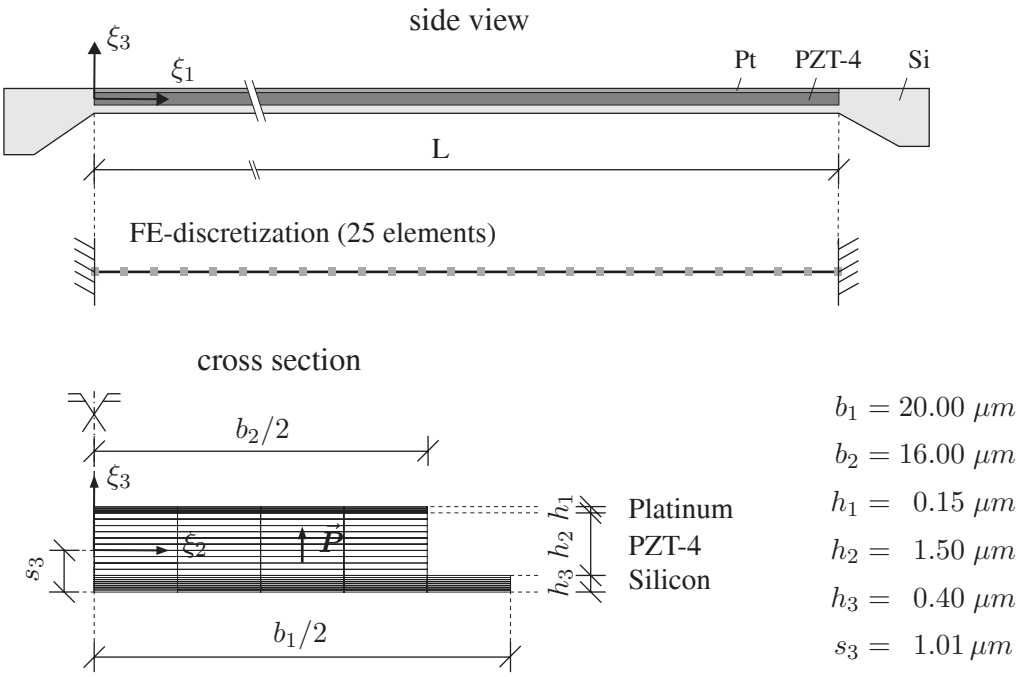

Figure 14: Configuration of the analyzed piezoelectric switch.

correspond with typical sizes reported in literature, see e.g. [16, 44]. The coordinates of the neutral axis $S(s_2, s_3)$ are computed under consideration of the different elastic moduli of the materials. It is located at $s_3 = 1.01$ μm with reference to the bottom line of the silicon layer, see Fig. 14. The piezoelectric layer is loaded with an electric voltage in ξ_3-direction with an increasing value between $0 - 2\ V$. Within the beam formulation the corresponding loading is realized with a prescribed degree of freedom c_3 for all nodes which is increased from 0 to $1.33 \cdot 10^6\ V/m$. The beam is discretisized with 26 elements. The resulting load-deflection-curve is given in Fig. 15 for different beam lengths. The nonlinear behavior of the structure can be seen clearly. Due to the eccentricity of the piezoelectric layer, a continuous transition to the post critical state can be found. If the loading reaches the critical value, a small load increment is sufficient to receive a relatively high displacement. This effect might be of interest for technical applications. Fig. 16 illustrates one half of the symmetric switch in the initial and in the deformed state.

layer	elastic modulus [GPa]	Poisson's ratio [-]	discretization $b \times h$
Platinum, Pt	250	0.25	8×4
PZT-4	see Appendix A.3		8×10
Silicon, Si	162	0.23	10×8

Table 3: Material data and discretization of each layer.

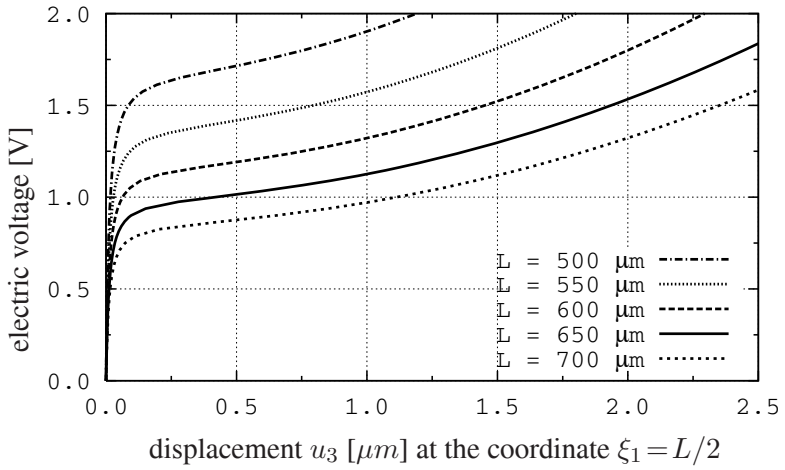

Figure 15: Load-deflection-diagram for different beam lengths L.

The discretization of the cross section with finite elements allows a detailed analysis of the stress distribution within the different materials. For instance, this can be used to analyze the compression stresses in the piezoelectric layer to avoid a ferroelastic depolarization. For this purpose we refer to a former publication [11] that treats the stress distribution in a switching device of the length 650 μm. These results show that the compression stresses are by approximately the factor of five smaller than the critical value of the coercive stress. Thus, no depolarization effects are expected within the device.

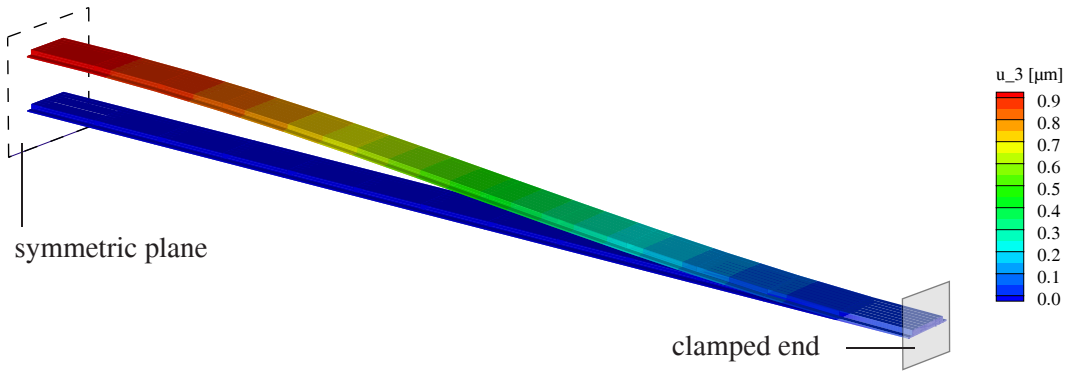

Figure 16: Plot of one half of the switch with $L = 650$ μm in the initial state and in the loaded state with $U = 1.2$ V, deflections scaled by factor 20.

7.5 Helical spring

A major drawback of piezoelectric actuators are the small displacements that can be achieved. For this reason, different concepts were developed to increase the maximum displacement amplitude, as described for instance by Niezrecki et al. [38]. Pearce et al. [41]

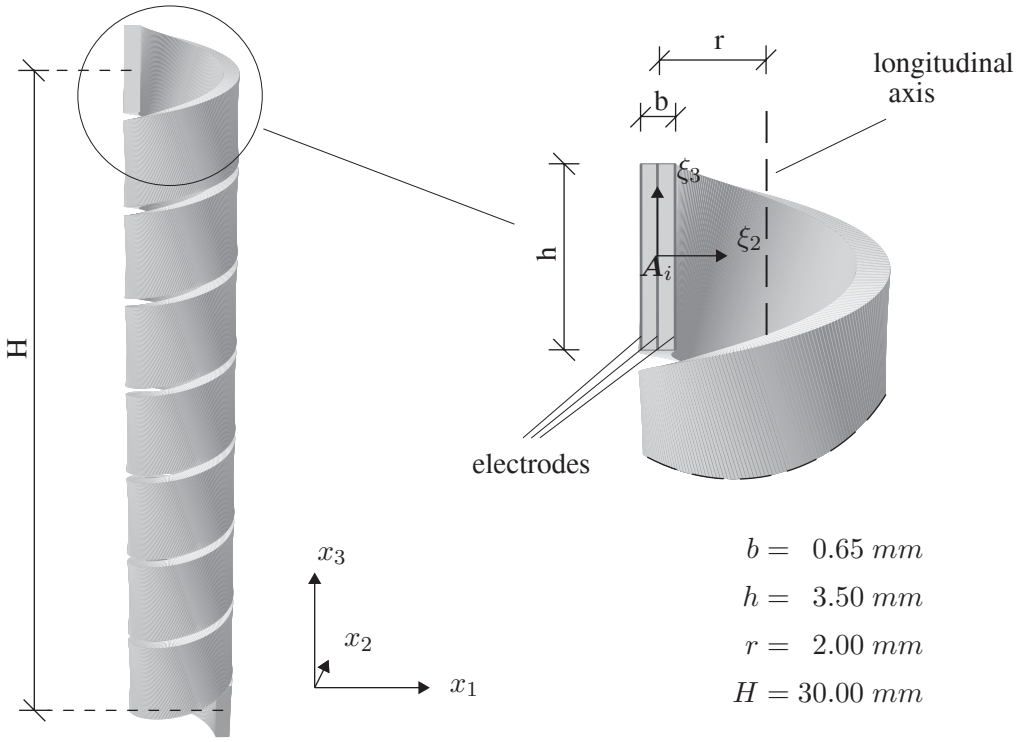

Figure 17: Configuration of the analyzed actuator.

propose a spiral shaped, piezoelectric actuator, which is shown in Fig. 17. This type of actuator allows to apply a displacement in longitudinal direction as well as a rotation about the longitudinal axis. Therefore, its cross section is divided in radial direction into two piezoelectric layer which are similarly poled. The electric field is applied in opposite direction on each layer and leads to converse strains in both materials. Consequently, the basic functional principle is equal to the classical bimorph actuator, see e.g. Poizat & Benjeddou [42].

The discussed actuator was already analytically and experimentally analyzed by Pearce et al. [41]. The configuration of the considered specimen is given in Fig. 17. Both piezoelectric layer are made of PZT-5H material which is polarized in local ξ_2-direction, the specific material parameter are given in Appendix A.4.

An important difference to the former examples is the fact that here two piezoelectric layers with different loading conditions are considered. Thus, the five degrees of freedom c_1 to c_5 of the numerical model are not sufficient to model this load case. This limitation can be by-passed using the eccentric formulation of the beam element. Therefore, the helical spring is discretisized with two beam elements in ξ_2-direction, one for each piezoelectric layer. The nodes of both beam elements must have the same spatial coordinates, which can be easily provided by the eccentric formulation, as illustrated in Fig. 18. Thus, it is possible to apply different loading conditions for each layer. To ensure the same kinematic of the adjacent

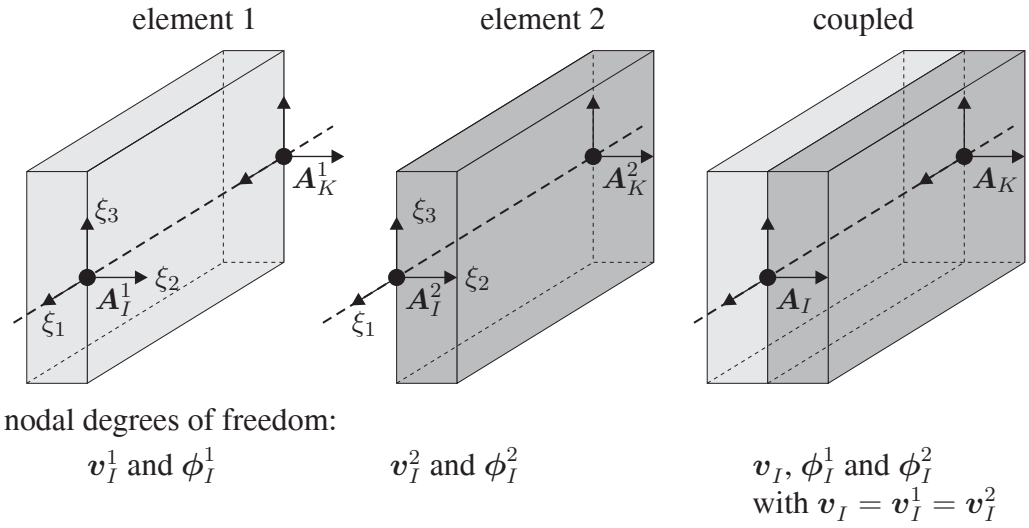

Figure 18: Consideration of two electric load cases within one cross section with coupled beam elements.

beam elements, the mechanical degrees of freedom are linked together within the numerical model. This leads to a numerical model with one set of mechanic degrees of freedom and two sets of electric degrees of freedom, one for each material. The main disadvantage of this procedure is that the cross section warping effects can not be considered. Since these effects are negligible in this example, the proposed approach is appropriate for the numerical model of this problem.

Each layer of the helical spring is discretisized with 135 elements for the numerical computation, see Fig. 19. From a preliminary analysis follows that this discretization is sufficient for the discussed problem [11]. To compare the numerical results with the analytical and the experimental data from literature, we consider the angle of rotation of the free end φ_3^E as defined in Fig. 19 for different values of $\vec{E}_2$.

The results of the linear finite element analysis coincide very well with the analytical solution. The small differences originate from different approximations of the electric potential within the cross section. While the analytical solution considers only a linear distribution of ϕ, the finite element model incorporates a quadratic one.

$\vec{E}^c$ [V/m]	$\vec{P}^{sat}$ [C/m^2]	E^{sat} [-]	c [-]	f_α [-]	f_β [-]	y_α [-]	y_β [-]
$0.65 \cdot 10^6$	0.330	0.00125	16.0756	8.0	8.0	0.50	-0.50

Table 4: Nonlinear material parameter for PZT-5H. The values for $\vec{E}^c$ and $\vec{P}^{sat}$ are taken from [10].

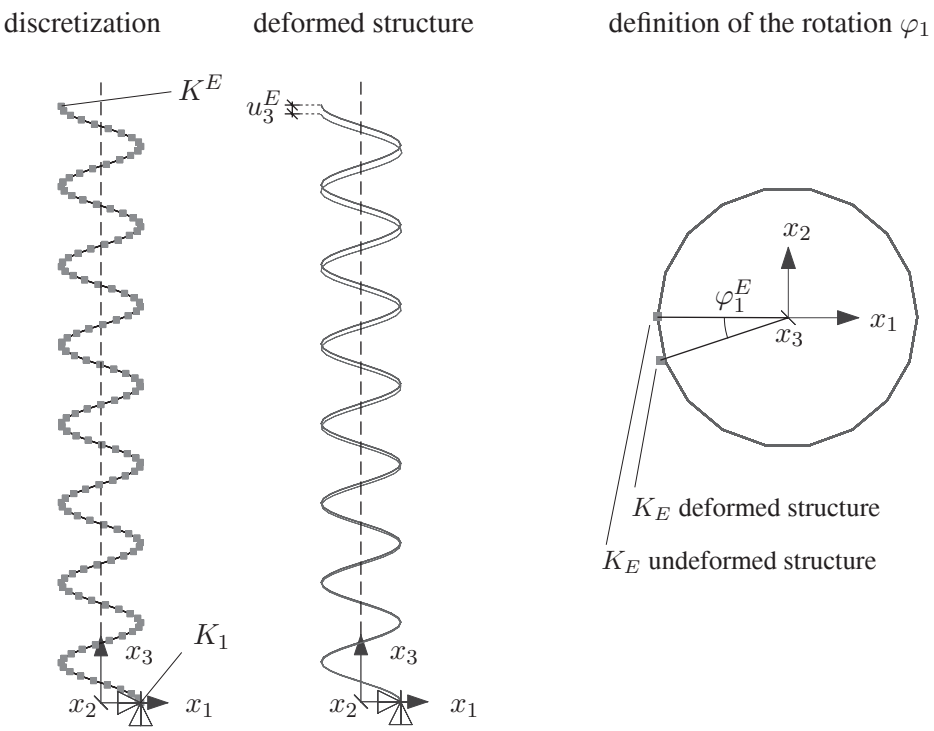

Figure 19: discretized actuator with 135 elements, and definition of the end displacement u_3^E and the end rotation φ_3^E.

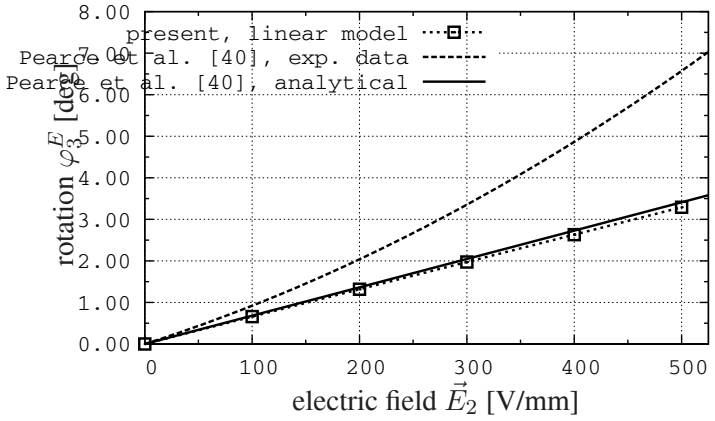

Figure 20: Comparison of the numerical results with approximated experimental data under consideration of a linear constitutive law.

As expected, the relation between φ_3^E and $\vec{E}_2$ is linear, as depicted in Fig. 20. However, there is obviously a great discrepancy to the data obtained by experimental measurements. These data can be approximated with a quadratic function as proposed by Pearce et al. [40]. A similar nonlinear behavior is reported by Mohammadi et [35] who attributes this observations to ferroelectric hysteresis effects.

To improve the numerical results, another finite element analysis is realized considering the

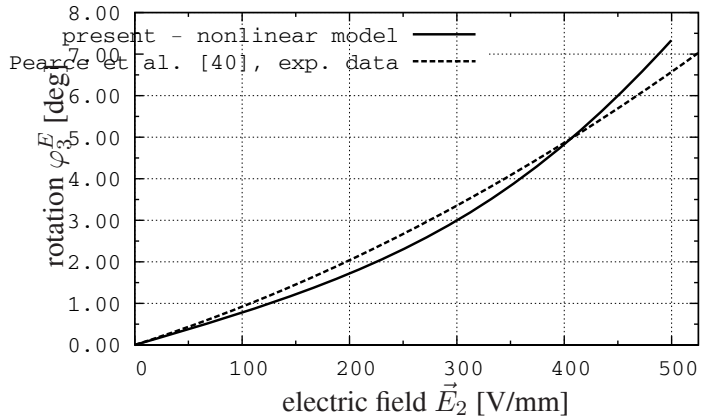

Figure 21: Comparison of the numerical results with approximated experimental data under consideration of the nonlinear Preisach model.

Preisach model to account for the nonlinear constitutive law. The additional material parameter are given in Tab. 4. In this case, the results show a relatively good agreement to the experimental data, see Fig. 21. The differences can be explained by the fact, that the used Preisach function does not correspond exactly to the hysteresis behavior of the PZT-5H material. A much better accordance is expected, if an experimentally determined Preisach function would be used in the numerical model.
This example illustrates again the applicability of the beam formulation which can also handle three dimensional problems in combination with nonlinear piezoelectric material effects.

8 CONCLUSIONS

In this paper a beam element is developed to analyze piezoelectric structures considering geometrical and material nonlinearities. The geometrically nonlinear beam kinematics are based on the Timoshenko beam assumptions, which are extended with three warping functions. Thus the formulation accounts for cross-section warping due to torsion and electric induced shear deformations. The material nonlinear behavior, which considers domain switching effects, is described by the Preisach model. A consistent finite element implementation is presented. The numerical example shows the applicability of the proposed element to nonlinear piezoelectric problems. The last example demonstrates that the presented beam formulation is able to simulate hystresis effects which are observed in a modern actuator device.

Acknowledgement: The work of the first author was supported by the Research Training Group 'Mixed Fields and Nonlinear Interactions' of the Deutsche Forschungsgemeinschaft (http://www.gkmf.uni-karlsruhe.de), which is gratefully acknowledged.

A Material data

The data are given in the following dimensions: $\mathbb{C}$ in [GPa], $\mathfrak{e}$ in [C/m^2] and $\boldsymbol{\epsilon}$ in [C^2/Nm^2].

A.1 Example 7.1

Piezoelectric material [26], polarized in ξ_3-direction
$\mathbb{C}_{11} = \mathbb{C}_{22} = \mathbb{C}_{33} = 128.4, \quad \mathbb{C}_{12} = \mathbb{C}_{21} = \mathbb{C}_{13} = \mathbb{C}_{31} = \mathbb{C}_{23} = \mathbb{C}_{32} = 69.1,$
$\mathbb{C}_{44} = \mathbb{C}_{55} = \mathbb{C}_{66} = 29.6, \quad \mathfrak{e}_{13} = \mathfrak{e}_{23} = -3.46, \quad \mathfrak{e}_{33} = 25.58, \quad \mathfrak{e}_{52} = \mathfrak{e}_{61} = 15.41,$
$\epsilon_{11} = \epsilon_{22} = \epsilon_{33} = 1.50 \cdot 10^{-8}$

A.2 Example 7.2 and 7.3

Material: PZT-5H [8], polarized in ξ_1-direction
$\mathbb{C}_{11} = \mathbb{C}_{22} = \mathbb{C}_{33} = 126.0, \quad \mathbb{C}_{12} = \mathbb{C}_{21} = \mathbb{C}_{13} = \mathbb{C}_{31} = 84.1,$
$\mathbb{C}_{23} = \mathbb{C}_{32} = 79.5 \quad , \mathbb{C}_{44} = \mathbb{C}_{55} = 23.0 \quad , \mathbb{C}_{66} = 23.3$
$\mathfrak{e}_{11} = 23.3, \quad \mathfrak{e}_{21} = \mathfrak{e}_{31} = -6.5, \quad \mathfrak{e}_{42} = \mathfrak{e}_{63} = 17.0, \quad \epsilon_{11} = 1.30 \cdot 10^{-8}, \epsilon_{22} = \epsilon_{33} = 1.503 \cdot 10^{-8}$

A.3 Example 7.4

Material: PZT-4, polarized in ξ_3-direction
$\mathbb{C}_{11} = \mathbb{C}_{22} = 138.5 \quad \mathbb{C}_{33} = 114.7, \quad \mathbb{C}_{12} = \mathbb{C}_{21} = 77.4$
$\mathbb{C}_{13} = \mathbb{C}_{31} = \mathbb{C}_{23} = \mathbb{C}_{32} = 73.6, \quad \mathbb{C}_{44} = 30.6 \quad , \mathbb{C}_{55} = \mathbb{C}_{66} = 25.6$
$\mathfrak{e}_{13} = \mathfrak{e}_{23} = -5.2, \quad \mathfrak{e}_{33} = 15.1, \quad \mathfrak{e}_{52} = \mathfrak{e}_{61} = 12.7, \quad \epsilon_{11} = \epsilon_{22} = 1.31 \cdot 10^{-8},$
$\epsilon_{33} = 1.15 \cdot 10^{-8}$

A.4 Example 7.5

Material: PZT-5H [10], polarized in $-\xi_2$-direction
$\mathbb{C}_{11} = \mathbb{C}_{22} = 126.0, \quad \mathbb{C}_{33} = 117.0 \; \mathbb{C}_{12} = \mathbb{C}_{21} = 79.5$
$\mathbb{C}_{13} = \mathbb{C}_{31} = \mathbb{C}_{23} = \mathbb{C}_{32} = 84.1, \quad \mathbb{C}_{44} = 23.5 \quad , \mathbb{C}_{55} = \mathbb{C}_{66} = 23.0$
$\mathfrak{e}_{12} = \mathfrak{e}_{22} = 6.55, \quad \mathfrak{e}_{32} = -23.3, \quad \epsilon_{11} = \epsilon_{22} = 2.77 \cdot 10^{-8}, \epsilon_{33} = 3.01 \cdot 10^{-8}$

References

[1] Aldraihem OJ, Khdeir AA. Smart Beams with Extension and Thickness-Shear Piezoelectric Actuators. *Smart Materials and Structures* 2000; **9**(1):1–9.

[2] Aldraihem OJ, Wetherhold, RC. Mechanics and Control of Coupled Bending and Twisting Vibration of Laminated Beams. *Smart Materials and Structures* 1997; **6**(2):123–133.

[3] Altay GA ,Dökmeci MC. Some Comments on the Higher Order Theories of Piezoelectric, Piezothermoelastic and Thermopiezoelectric Rods and Shells. *International Journal of Solids and Structures* 2003; **40**(18):4699–4706.

[4] Baillargeon, BP ,Vel SS. Active Vibration Suppression of Sandwich Beams using Piezoelectric Shear Actuators: Experiments and Numerical Simulations. *Journal of Intelligent Material Systems and Structures* 2005; **16**(6):517–530.

[5] Barker JA ,Schreiber DE ,Huth BG ,Everett DH. Magnetic Hysteresis and Minor Loops: Models and Experiments. *Proceedings of the Royal Society of London. Series A.* 1983; **386**(1791):251–261.

[6] Benjeddou A. Advances in Piezoelectric Finite Element Modeling of Adaptive Structural Elements: A Survey. *Computers & Structures* 2000; **76**:347–363.

[7] Benjeddou A. Use of Shear-Mode Piezoceramics in Smart Structures Applications: Archievements and Perspectives. In: *Second Eccomas Thematic Conference on Smart Structures and Materials*, ECCOMAS, 2005.

[8] Benjeddou A, Trindade MA, Ohayon R. A Unified Beam Finite Element Model for Extension and Shear Piezoelectric Actuation Mechanims. *Journal of Intelligent Material Systems and Structures* 1997; **8**(12):1012–1025.

[9] Benjeddou A, Trindade MA, Ohayon R. New Shear Actuated Smart Structure Beam Finite Element. *AIAA Journal* 1999; **37**(3):378–383.

[10] Berlincourt D, Krueger HHA. Morgan Electro Ceramics Technical Publication TP-226. Properties of Piezoelectric Ceramics. *http://www.morganelectroceramics.com/.*

[11] Butz, A. Nichtlineare Formulierung piezoelectrischer 3D-Stabstrukturen - Theorie und Finite-Element-Modellierung. Dissertation, Institut für Baustatik, Universität Karlsruhe (TH), Germany, *Report* **11** 2006.

[12] Butz A, Klinkel S, Wagner W. A Nonlinear Piezoelectric 3D-Beam Finite Element Formulation. In: BATHE, K.J., (HRSG.), *Computational Fluid and Solid Mechanics* 2005 121–126.

[13] Chróścielewski J, Klosowski P, Schmidt R. Modelling and FE-Analysis of Large Deflection Shape and Vibration Control of Structures via Piezoelectric Layers. In: GABBERT, U., (HRSG.), *Smart Mechanical Systems - Adaptronics*, Düsseldorf, 1997 VDI Verlag, 1997; 53–61.

[14] Cima L, Laboure E. Characterization and Model of Ferroelectrics Based on Experimental Preisach Density. *Review of Scientific Instruments* 2002; **73**(10):3546–3552.

[15] DeVoe, DL, Pisano AP. Modeling and Optimal Design of Piezoelectric Cantilever Microactuators. *Journal of Microelectromechanical Systems* 1997; **6**(3):266–270.

[16] DeVoe DL, Pisano AP. Surface Micromachined Piezoelectric Accelerometers (PiXLs). *Journal of Microelectromechanical Systems* 2001; **10**(2):180–186.

[17] Ganapathi M, Patel BP, Touratier M. Refined Finite Element for Piezoelectric Laminated Composite Beams. *Smart Materials and Structures* 2004; **13**(4):N57–N67.

[18] Gross SJ, Tadigadapa S, Jackson TN, Troiler-McKinstry S, Zhang QQ. Lead-Zirconate-Titanate-Based Piezoelectric Micromachined Switch. *Applied Physics Letters* 2003; **83**(1):174–176.

[19] Gruttmann F, Sauer R, Wagner W. A Geometrical Nonlinear Eccentric 3D–Beam Element with Arbitrary Cross–Sections. *Computer Methods in Applied Mechanics and Engineering* 1998; **160**(3–4):383–400.

[20] Gruttmann, F, Sauer R, Wagner W. Shear Stresses in Prismatic Beams with Arbitray Cross-Sections. *International Journal for Numerical Methods in Engineering* 1999; **45**(7):865–889.

[21] Gruttmann F, Sauer R, Wagner W. Theory and Numerics of Three-Dimensional Beams with Elastoplastic Material Behaviour. *International Journal for Numerical Methods in Engineering* 2000; **48**(12):1675–1702.

[22] Hu YT, Yang JS, Jiang Q. Characterisation of Electroelastic Beams under Biasing Fields with Applications in Buckling Analysis. *Archive of Applied Mechanics* 2002; **72**:439–450.

[23] Hwang SC, Lynch CS, McMeeking RM. Ferroelectric/Ferroelastic Interactions and a Polarisation Switching Model. *Acta Metallurgica et Materialia* 1995; **43**(5):2073–2084.

[24] Iyer RV, Shirley ME. Hysteresis Parameter Identification With Limited Experimental Data. *IEEE Transactions on Magnetics* 2004; **40**(5):3227–3239.

[25] Jiao BL, Zhang JD. Torsional Modes in Piezo Helical Springs. *IEEE Transactions on Ultrasonics, Ferroelectrics and Frequency Control* 1999; **46**(1):147–151.

[26] Kamlah M. Ferroelectric and Ferroelastic Piezoceramics - Modeling of Electromechanical Hysteresis Phenomena. *Continuum Mechanics and Thermodynamics* 2001; **13**:219–268.

[27] Klinkel S. A phenomenological constitutive model for ferroelastic and ferroelectric hysteresis effects in ferroelectric ceramics. *International Journal for Solids and Structures* 2006; **43**:7197–7222.

[28] Klinkel S, Govindjee S. Anisotropic Bending-Torsion Coupling for Warping in a Non-Linear Beam. *Computational Mechanics* 2003; **31**(1):78–87.

[29] Krasnosel´skii MA, Pokrovskiĭ AV. *Systems with Hysteresis.* Springer-Verlag, Berlin/Heidelberg, 1989.

[30] Krommer M, Irschik H. An Electromechanically Coupled Theory for Piezoelastic Beams taking into Account the Charge Equations of Electrostatics. *Acta Mechanica* 2002; **154**:141–158.

[31] Landis CM. Fully Coupled, Multi-axial, Symmetric Constitutive Laws for Polycrystalline Ferroelectric Ceramics. *Journal of the Mechanics and Physics of Solids* 2002; **50**:127–152.

[32] Linnemann K, Klinkel S. A Mixed Finite Element Formulation for Piezoelectric Materials. *Proceedings in Applied Mathematics and Mechanics* 2005; **5**(1):425–426.

[33] Mayergoyz ID. *Mathematical Models of Hysteresis and Their Applications.* Elsevier Series in Electromagnetism Elsevier, 2003.

[34] McMeeking RM, Landis CM. A Phenomenological Multiaxial Constitutive Law for Switching in Polycrystalline Ferroelectric Ceramics. *International Journal of Engineering Science* 2002; **40**:1553–1577.

[35] Mohammadi F, Kholkin AL, Jadidian B, Safri A. High-displacement Spiral Piezoelectric Actuators. *Applied Physics Letters* 1999; **75**(16):2488–2490.

[36] Mukherjee M, Chaudhuri AS. Active Control of Dynamic Instability of Piezolaminated Imperfect Columns. *Smart Materials and Structures* 2002; **11**(6):874–879.

[37] Mukherjee M, Chaudhuri AS. Piezolaminated Beams with Large Deformations. *International Journal of Solids and Structures* 2002; **39**:4567–4582.

[38] Niezrecki C, Brei D, Balakrishnan S, Moskalik A. Piezoelectric Actuation: State of the Art. *The Shock and Vibration Digest* 2001; **33**(4):269–280.

[39] Pasco Y, Berry A. A Hybrid/Numerical Model of Piezoelectric Stack Actuators Using a Macroscopic Nonlinear Theory of Ferroelectricity and a Preisach Model of Hysteresis. *Journal of Intelligent Material Systems and Structures* 2004; **15**(5):375–386.

[40] Pearce DH, Hooley A, Button TW. On Piezoelectric Super-Helix Actuators. *Sensors and Actuators* 2002; **A 100**:281–286.

[41] Pearce DH, Seffen KA, Button TW. Net Shape Formed Spiral and Helical Piezoelectric Actuators. *Journal of Materials Science* 2002; **37**:3117–3122.

[42] Poizat C, Benjeddou A. On Analytical and Numerical Modelling of Piezoelectric Bimorphs. In: TOPPING, B.V.H. / MOTA SOARES, C.A., (HRSG.), *Proceedings of the Seventh International Conference on Computational Structures Technology*, Stirling, Scotland, 2004 Civil-Comp. Press.

[43] Preisach F. Über die magnetische Nachwirkung. *Zeitschrift für Physik* 1935; **94**:277–302.

[44] Saif MTA. On a Tunable Bistable MEMS-Theory and Experiment. *Journal of Microelectromechanical Systems* 2000; **9**(2):157–170.

[45] Saravanos DA, Heyliger PR. *Coupled Layerwise Analysis of Composite Beams with Embedded Piezoelectric Sensors and Actuators. Journal of Intelligent Material Systems and Structures* 1995; **6**(3):350–363.

[46] Saravanos DA, Heyliger PR. Mechanics and Computational Models for Laminated Piezoelectric Beams, Plates, and Shells. *Applied Mechanics Reviews* 1999; **52**(10):305–320.

[47] Sauer R. *Eine einheitliche Finite-Element-Formulierung für Stab- und Schalentragwerke mit endlichen Rotationen.* Dissertation, Institut für Baustatik, Universität Karlsruhe (TH), Germany, *Report* **4** 1998.

[48] Senturia SD. *Microsystem Design.* Kluwer Academic Publishers, Boston/ Dordrecht/ London, 2001.

[49] Simkovics R, Landes H, Kaltenbacher M, Hoffelner J, Lerch R. *Finite Element Analysis of Hysteresis Effects in Piezoelectric Transducers.* In: *Proc. SPIE, Smart Structures and Materials 2000: Mathematics and Control in Smart Structures, Vasundara V. Varadan; Ed.*, 2000 **3984**:33–44.

[50] Smith RC. *Smart Material Systems: Model Development.* Frontiers in Applied Mathematics SIAM, New York, 1. Auflage, 2005.

[51] Smits JG, Fujimoto K, Kleptsyn VF. Microelectromechanical Flexure PZT Actuated Optical Scanner: Static and Resonance Behavior. *Journal of Micromechanics and Microengineering* 2005; **15**(6):1285–1293.

[52] Stuelpnagel J. On the Parametrization of the Three-Dimensional Rotation Group. *SIAM Review* 1964; **6**(4):422–430.

[53] Sun CT, Zhang XD. Use of Thickness-shear Mode in Adaptive Sandwich Structures. *Smart Materials and Structures* 1995; **4**(3):202–206.

[54] Tani J, Takagi T, Qiu J. Intelligent Material Systems: Application of Functional Materials. *Applied Mechanics Reviews* 1998; **51**(8):505–521.

[55] Taylor RL. *FEAP Manual.* http://www.ce.berkeley.edu/ rlt/feap/, 2003.

[56] Timoshenko SP, Goodier JN. *Theory of Elasticity.* McGraw-Hill, New York, 3. Auflage, 1970.

[57] Tressler JF, Alkoy S, Newnham RE. Piezoelectric Sensors and Sensor Materials. *Journal of Electroceramics* 1998; **2**(4):257–272.

[58] Wang Q, Quek T. Flexural Vibration Analysis of Sandwich Beam Coupled with Piezoelectric Actuator. *Smart Materials and Structures* 2000; **9**(1):103–109.

[59] Wang Q, Quek T. *A Model for the Analysis of Beams with Embedded Piezoelectric Layers. Journal of Intelligent Material Systems and Structures* 2002; **13**(1):61–70.

[60] Yu Y, Naganathan N, Dukkipati R. Preisach Modeling of Hysteresis for Piezoceramic Actuator System. *Mechanism and Machine Theory* 2002; **37**:49–59.

[61] Zhang XD, Sun CT. Formulation of an Adaptive Sandwich Beam. *Smart Materials and Structures* 1996; **5**(6):814–823.